arXiv:2012.00561v1 [cond-mat.stat-mech] 1 Dec 2020

Equilibrium and dynamical phase transitions in fully connected quantum Ising model: Approximate energy eigenstates and critical time

Arun Sehrawat,[1,2,*] Chirag Srivastava,[1,†] and Ujjwal Sen[1,2,‡]

[1] *Harish-Chandra Research Institute, HBNI, Chhatnag Road, Jhunsi, Allahabad 211019, India*
[2] *QpiAI India Pvt Ltd, WeWork, Bellary Road, Hebbal, Bengaluru 560024, India*

(Dated: December 1, 2020)

We study equilibrium as well as dynamical properties of the finite-size fully connected Ising model with a transverse field at the zero temperature. In relation to the equilibrium, we present approximate ground and first excited states that have large overlap—except near the phase transition point—with the exact energy eigenstates. For both the approximate and exact eigenstates, we compute the energy gap, concurrence, and geometric measure of quantum entanglement. We observe a good match in the case of energy gap and geometric entanglement between the approximate and exact eigenstates. Whereas, when the system size is large, the concurrence shows a nice agreement only in the paramagnetic phase. In a quench dynamics, we study the time period and the first critical time, which play important roles in the dynamical phase transitions, based on a dynamical order parameter and the Loschmidt rate, respectively. When all the spins are initially polarized in the direction of their mutual interaction, both the time period and critical time diverges logarithmically with the system size at the dynamical critical point. When all the spins are initially in the direction of transverse field, both the time period and critical time exhibit logarithmic or power-law divergences depending on the final field strength. In the case of convergence, we provide estimates for the finite-size scaling and converged value.

I. INTRODUCTION

Quantum phase transitions are one of the most fascinating phenomena that emerge in many-body systems at zero temperature in the thermodynamic limit [1]. In this paper, we study phase transitions for the fully connected Ising model (FCIM) with a transverse magnetic field. It is a special case of the Lipkin-Meshkov-Glick (LMG) model [2–4] and is related to the two-component Bose-Einstein condensates [5, 6]. Ferromagnetic to paramagnetic equilibrium phase transition occurs in the FCIM as we increase the field strength from zero to infinity. The transition can be described by adopting a mean-field approach [7–9] (see also [5]).

The finite-size scaling analysis of [10] is extended in [7, 8] for the LMG Model, and it is shown how the magnetization and energy gap approach their mean-field values as the system size grows. At the critical point, they go to zero with a *power-law*. One needs to go beyond mean-field theory to capture entanglement properties such as concurrence [11, 12] and geometric entanglement [13–27] of the ground state. The rescaled concurrence develops a cusp-like singularity at the critical point with a power-law [28–31]. Whereas, the geometric entanglement [32], entanglement entropy [33–35], and mutual information [36] of the ground state diverge *logarithmically* with system size at the phase transition point. The finite-size scaling exponents for two-body correlations are obtained in [30, 37] for the LMG model.

In Sec. II, we consider certain approximate ground and the first excited state-vectors, for the FCIM, which are obtained within an improvisation of the mean-field approach, suggested in [5]. By computing their overlaps with the associated exact energy eigenkets, we realize that they provide good approximations for a finite system except near the equilibrium critical point. We also obtain the rescaled concurrence and geometric entanglement for both the approximate and exact energy eigenkets and compare the results. In the case of concurrence, we observe a good match only in a certain parameter range. While for the geometric entanglement and energy gap, we witness overall a good agreement excluding a small interval around the critical point.

In Sec. III, we investigate dynamical phase transitions (DPTs) in the FCIM through a quantum quench, where a value of a Hamiltonian parameter (the transverse field strength in our case) is abruptly changed, and thus the system goes out of equilibrium and the dynamics begin. Broadly, the DPTs are of two kinds, viz. the first and second kinds - DPT-I [9, 38–58, 62, 70, 74] and DPT-II [52, 57, 59–75] - and are based on a certain dynamical order parameter and the Loschmidt rate function, respectively. In the case of FCIM, the equilibrium phase transition and DPTs are distinct phenomena and their critical points are different [53, 69, 70, 72]. Recently, DPTs have been experimentally realized in [55–57, 59] for the FCIM and LMG model, and in [58] for the collective Heisenberg model. It should be noted that the name, "dynamical phase transition", has been used also for phenomena somewhat independent of the one considered in this paper [76–80].

Like an equilibrium phase transition, two phases in a DPT-I are associated with nonzero and zero values of a dynamical order parameter, and how it goes to zero at

* arunsehrawat2@gmail.com
† chiragsrivastava@hri.res.in
‡ ujjwal@hri.res.in

the critical point determines the nature of the transition. The DPT-I in the Fermi–Hubbard model [43–45], Bose–Hubbard model [46–48], Jaynes–Cummings model [48], quantum ϕ^4 N-component field theory [49], films [50], and in the FCIM [9, 48, 51–54] are described through classical (mean-field) equations of motion in the thermodynamic limit, where an order parameter oscillates around its time-averaged value with a time period. The averaged value is called the *dynamical* order parameter. Furthermore, it is known that the time period and dynamical order parameter, respectively, go to infinity and zero *logarithmically*—in contrast to the equilibrium phase transitions—as functions of the Hamiltonian parameter at the dynamical critical point. We shall see in the Sec. III A 1 that these two physical quantities are inversely proportional to each other in the FCIM [54], and the time period diverges logarithmically with the system size at the critical point, which is one of our contributions.

In the case of DPT-II, the Loschmidt rate—as a function of time and the Hamiltonian parameter—is a dynamical counterpart of the free energy density, and a sharp change in its behavior indicates a phase transition [60, 75]. The change can be observed with respect to the Hamiltonian parameter (for example, see [69, 70]) or related to time [59, 62].

If one examines the behavior of Loschmidt rate (considering all the times) with respect to the Hamiltonian parameter, then she will observe the regular and anomalous phases when the quenching is from the ferromagnetic phase and will observe the regular and trivial phases when it is from the paramagnetic phase in the FCIM [69–71] (for further analyses, see [52, 72–74]). Subsections III A and III B separately deals with the quantum quenching from the ferromagnetic and paramagnetic phases, respectively. In each of these subsections, we study the DPT-I and DPT-II sequentially.

For a fixed Hamiltonian-parameter value, the rate can show a series of kinks or cusps (non-analyticities) at the so-called critical times. There is no cusp in the trivial phase. The regular and anomalous phases have the first cusp before and after the first minimum of the rate function, respectively. In this paper, we study the *first* critical time (when the first kink occurs). The time period and the critical time share a close relationship [52, 59, 60, 62, 70, 72]. In Sec. III, as a set of results, we essentially show that both the time period and the first critical time have the same diverging behavior (logarithmic or power-law) with respect to system size at the critical points. In a convergent case, we provide estimates for the finite-size scaling and converged value for both the time period and critical time. Our main results are highlighted at the beginning of each subsection, and a summary is presented in Sec. IV. Appendices carry the supplementary material.

II. APPROXIMATE GROUND AND EXCITED STATES AND THEIR PROPERTIES

In this section, we set the stage by presenting some known results about the equilibrium phase transition in the FCIM. Then, as our first result of this section, we provide justifications for (14), which basically says that for a finite system, the approximate energy eigenkets $|\chi\rangle$ of (8) and (12) are better than the mean-field approximations of the exact energy eigenkets $|e\rangle$ except near the phase transition point. Our justifications are based on the numerical data plotted in Figs. 1, 2, 3, and 18. As our second contribution, we capture the entanglement properties of $|e\rangle$ through $|\chi\rangle$, which are presented in (16), (18), (19), and Figs. 4 and 5. Now we begin our analysis.

For a system of N spin-$\frac{1}{2}$ particles, $S_\eta := \frac{1}{2}\sum_{i=1}^{N}\sigma_i^\eta$ specifies the total angular momentum in the direction $\eta = x, y, z$, where the Pauli operator σ_i^η acts on the ith spin only. The square of the angular momentum operator, $(S_z)^2 = \frac{1}{4}\sum_{i,k=1}^{N}\sigma_i^z\sigma_k^z$, describes a symmetric two-body interaction between each pair of particles. The Hamiltonian of the FCIM with a transverse field is given by

$$H = -\frac{\Gamma}{2N}(S_z)^2 - h\,S_x\,, \tag{1}$$

where Γ and h are the two-body interaction and transverse-field strengths, respectively. The Hamiltonian commutes with $\mathbf{S}^2 = \mathbf{S}\cdot\mathbf{S}$, where $\mathbf{S} = (S_x, S_y, S_z)$, and with the spin-flip operator $X := \otimes_{i=1}^{N}\sigma_i^x$ [30]:

$$[H, \mathbf{S}^2] = 0 = [H, X]\,. \tag{2}$$

The operators $\mathbf{S}^2$ and X also commute with each other.

At the zero temperature, for a ferromagnetic coupling $\Gamma > 0$, the ground state-vector $|e_0\rangle$ lies in the eigenspace,

$$\mathcal{S} = \text{span}(\mathcal{B}_z), \quad \mathcal{B}_z = \{\,|m\rangle_z\,\}_{m=-j}^{j}\,, \tag{3}$$

of $\mathbf{S}^2$ spanned by the Dicke kets [81] (see (A1) for their explicit forms). The eigenspace corresponds to the eigenvalue $j(j+1)$ of $\mathbf{S}^2$, where $j = \frac{N}{2}$. Throughout the paper, we fix the temperature to be zero and work with the unit-free Hamiltonian H/Γ instead of H, whereby our control parameter is the dimensionless quantity h/Γ. Moreover, we rename H/Γ as H and h/Γ as h, which is equivalent to setting $\Gamma = 1$.

Since the Hamiltonian commutes with $\mathbf{S}^2$, j remains conserved in a dynamics generated by H (as in Sec. III). So, in the paper, we only need the restricted Hamiltonian on the corresponding eigenspace:

$$\begin{aligned} \widehat{H} := H\big|_{\mathcal{S}} &= -\frac{1}{2N}(J_z)^2 - h\,J_x\,, \quad \text{where} \\ J_\pm\,|m\rangle_z &= \sqrt{(j\mp m)(j\pm m+1)}\;|m\pm 1\rangle_z\,, \\ J_z\,|m\rangle_z &= m\,|m\rangle_z\,, \end{aligned} \tag{4}$$

$J_\pm = J_x \pm \mathrm{i}J_y$, and $\mathbf{S}|_{\mathcal{S}} =: \mathbf{J} = (J_x, J_y, J_z)$. As the dimension $N+1$ of the subspace $\mathcal{S}$ grows linearly with the

system size N, it is easy to numerically diagonalize $\widehat{H}$ for a large j.

In this paragraph, we present the mean field (semi-classical) analysis borrowed from [5, 7–9, 30, 82] for the thermodynamic limit $N \to \infty$, which is the classical limit $j \to \infty$ in the FCIM. So, in this limit, we can find the ground state energy per particle by minimizing

$$\begin{aligned}\mathscr{E}_h(\theta,\phi) &:= \lim_{j\to\infty} \frac{\langle\theta,\phi|H|\theta,\phi\rangle}{j} \\ &= -\frac{1}{4}(\cos\theta)^2 - h\sin\theta\cos\phi \end{aligned} \tag{5}$$

over $\theta \in [0,\pi]$ and $\phi \in [0,2\pi)$, where

$$|\theta,\phi\rangle = \sum_{m=-j}^{j} \binom{2j}{j+m}^{\frac{1}{2}} \left(\cos\tfrac{\theta}{2}\right)^{j+m} \left(\sin\tfrac{\theta}{2}\, e^{\mathrm{i}\phi}\right)^{j-m} |m\rangle_z \,, \tag{6}$$

is the spin coherent ket [83] that represents all the spins are pointing in the same direction characterized by the angles θ and ϕ [see (A1)]. In (6), $\binom{2j}{j+m}$ is the binomial coefficient and $\mathrm{i} = \sqrt{-1}$. Both the coherent kets $|\theta_0,\phi_0\rangle$ and $|\pi-\theta_0,\phi_0\rangle$ provide the minimum energy $\mathscr{E}_h(\theta_0,\phi_0)$, where

$$(\theta_0,\phi_0) = \begin{cases} (0,\phi_0) & \text{for } h = 0 \\ (\arcsin(2h),0) & \text{for } 0 < 2h \leqslant 1 \\ (\tfrac{\pi}{2},0) & \text{for } 1 \leqslant 2h < \infty \end{cases} . \tag{7}$$

Since ϕ_0 does not depend on the parameter h, we simply write the kets as $|\theta_0\rangle$ and $|\pi-\theta_0\rangle$. One can observe that the kets are distinct in the ferromagnetic phase characterized by $0 \leqslant 2h < 1$. It indicates double degeneracy in the ground state. In the case of $h = 0$, the ground state is two-fold degenerate for every j, and $\mathrm{span}\{|\pm j\rangle_z\}$ is the corresponding energy eigenspace. Whereas, in the case of $0 < 2h < 1$, the ground state becomes "truly" degenerate only in the thermodynamic limit [7, 8, 30, 82]. The two coherent kets become the same $|\frac{\pi}{2}\rangle$ at the equilibrium phase transition point $h^{\mathrm{eq}} = \frac{1}{2}$ and remain so in the whole paramagnetic phase specified by $1 < 2h$. This reveals that the ground state is nondegenerate in the paramagnetic phase.

From here till Eq. (11), we are taking the case $0 < 2h < 1$ and $j < \infty$. The two coherent kets mentioned above are the zeroth-order approximations of $|e_0\rangle$ [30, 82]. In a realistic scenario, where we have a finite number of spins, the exact energy eigenkets $|e_{0,1}\rangle$ of $\widehat{H}$ are obtained numerically (the subscripts 0 and 1 are for the ground and first excited states). To see how well the approximation works, we plot the overlaps $|\langle\theta_0|e_0\rangle|^2$ as well as $|\langle\theta_0|e_1\rangle|^2$ as functions of j for fixed h-values in Figs. 1 and 18, and as functions of h for a fixed j-value in Fig. 2. The overlap measures the closeness of two quantum states, and it is unity (zero) if and only if the two states are the same (mutually orthogonal).

One can observe: **(i)** both the overlaps are not unity but close to one-half if we neglect small j-values in the case of $h = 0.4$ in Fig. 1 [see also Fig. 2]. The same is true if we pick the other coherent ket $|\pi-\theta_0\rangle$. **(ii)** As the ground and first excited states are non-degenerate for a finite j and $0 < h$ [7, 8, 30], they must be eigenstates of the spin-flip operator X according to the second commutator in (2). With $X|m\rangle_z = |-m\rangle_z$ and then $X|\theta_0\rangle = |\pi-\theta_0\rangle$, one can realize that neither of the two mean-field coherent kets is an eigenket of X but

$$|\chi_\pm\rangle := \frac{|\theta_0\rangle \pm |\pi-\theta_0\rangle}{\sqrt{2(1\pm(\sin\theta_0)^N)}} \in \mathcal{E}_\pm \quad \text{for} \quad 0 \leqslant 2h < 1 \tag{8}$$

are [5]. Moreover, the two coherent kets are neither same nor mutually orthogonal because $\langle\theta_0|\pi-\theta_0\rangle = (\sin\theta_0)^N$, whereas $\langle\chi_+|\chi_-\rangle = 0$. The operator X owns only two distinct eigenvalues ±1, and $\mathcal{E}_\pm$ are the associated eigenspaces. **(iii)** One can check that the exact energy eigenkets $|e_0\rangle \in \mathcal{E}_+$ and $|e_1\rangle \in \mathcal{E}_-$.

Based on the three observations, $|\chi_+\rangle$ seems to be a better approximate of $|e_0\rangle$ than the mean-field kets for a finite N and $0 < 2h < 1$. It is also suggested in [5]. To test this hypothesis, we plot the overlaps $|\langle\chi_+|e_0\rangle|^2$ and $|\langle\chi_-|e_1\rangle|^2$ as functions of j in Fig. 1, and it is justified in

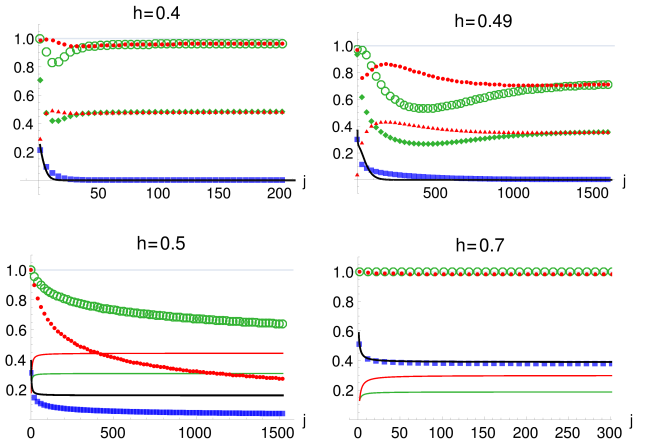

FIG. 1. Overlap versus system size. The top- and bottom-row-plots are for $2h < 1$ (ferromagnetic) and $1 \leqslant 2h$ (paramagnetic), correspondingly. The green circles (○) denote $|\langle\chi_+|e_0\rangle|^2$ and $|\langle\chi_0|e_0\rangle|^2$ in the top- and bottom-row-plots, respectively. Likewise, the red points (●) exhibit $|\langle\chi_-|e_1\rangle|^2$ in the top-plots and $|\langle\chi_1|e_1\rangle|^2$ in the bottom-plots as functions of j. In the top panels for $h = 0.4, 0.49$, the green diamonds (♦) and red triangles (▲) express $|\langle\theta_0|e_0\rangle|^2$ and $|\langle\theta_0|e_1\rangle|^2$, correspondingly. In all the pictures, the blue squares (■) represent the exact energy gap Δ between the ground and first excited states, and the black curves represent the approximate energy gap: Δ_{app} from (10) for $2h < 1$ and $\varepsilon_1 - \varepsilon_0$ from (B3) and (B4) for $1 \leqslant 2h$. The green and red curves in the bottom-row-plots illustrate $\frac{\mu_0}{2}$ and $\frac{\mu_1}{2}$ [given in (B3) and (B4)], respectively. In Fig. 18, more such plots are given for h close to the transition point.

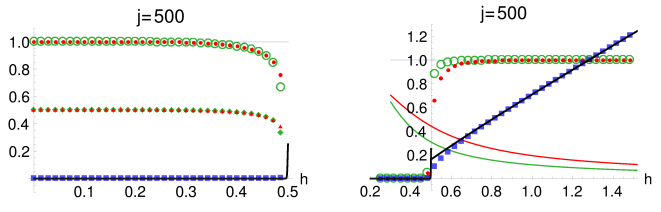

FIG. 2. Overlap versus external field strength. The left- and right-hand-side pictures are for $2h < 1$ (ferromagnetic) and $1 \leqslant 2h$ (paramagnetic), respectively. Here the only difference with respect to Fig. 1 is that the system size $2j$ is fixed and the same quantities are presented as functions of the field strength h.

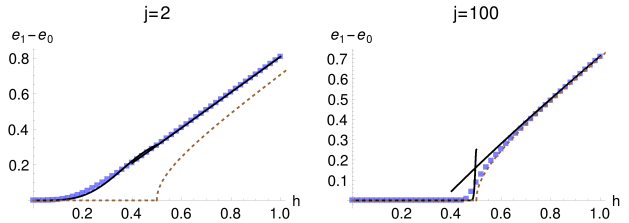

FIG. 3. Energy gap versus external field strength. The exact energy difference $\Delta = e_1 - e_0$ is illustrated by the blue squares (■) for two different system sizes [for $j = 500$, see Fig. 2]. The black curves represent $\Delta_{\rm app}$ for $0 \leqslant 2h < 1$ and $(\varepsilon_1 - \varepsilon_0)$ for $1 \leqslant 2h$. $\Delta_{\rm app}$, ε_0, and ε_1 are given in (10), (B3), and (B4), respectively. The brown dotted curve depicts—0 for $0 \leqslant 2h < 1$ and $\sqrt{h(h-1/2)}$ for $1 \leqslant 2h$—that is a result from [8] for the gap in the classical limit.

Appendix A that

$$\sqrt{\tfrac{1+(2h)^{2j}}{2}}\,\langle\chi_+|e_0\rangle = \langle\theta_0|e_0\rangle = \langle\pi-\theta_0|e_0\rangle \quad \text{and}$$
$$\sqrt{\tfrac{1-(2h)^{2j}}{2}}\,\langle\chi_-|e_1\rangle = \langle\theta_0|e_1\rangle = -\langle\pi-\theta_0|e_1\rangle\,. \qquad (9)$$

As $|\langle\chi|e\rangle| \geqslant |\langle\theta_0|e\rangle|$, indeed $|\chi\rangle$ is a better approximate of $|e\rangle$.

In Fig. 1, one can also notice that both the overlaps $|\langle\chi_+|e_0\rangle|^2$ and $|\langle\chi_-|e_1\rangle|^2$ are close to one once we neglect first few values of j in the case of $h = 0.4$. The overlaps show the same behavior for $h = 0.49$ but we may need to ignore more j-values to see them getting closer to one. For a large system size [see Fig. 2] the two overlaps stay close to one as long as we do not go very near to the phase transition point [see also Fig. 18]. So, in the ferromagnetic case, once we neglect small j-values, then we can make the approximations $|e_0\rangle \approx |\chi_+\rangle$ and $|e_1\rangle \approx |\chi_-\rangle$ for $j < \infty$ in the sense that $|\langle\psi|\psi'\rangle|^2 \approx 1$ implies $|\psi'\rangle\langle\psi'| \approx |\psi\rangle\langle\psi|$. Furthermore, in the whole span of $\{|\chi_\pm\rangle\}$, $|\chi_+\rangle$ and $|\chi_-\rangle$ are the only kets that provide the maximum overlaps with the exact ground and first excited state-vectors, respectively. Since $\mathcal{E}_+$ and $\mathcal{E}_-$ are mutually orthogonal invariant subspaces of Hamiltonian (1), H is diagonal in the orthonormal basis $\{|\chi_\pm\rangle\}$ of a 2-dimensional subspace, and

$$\Delta_{\rm app} := \langle\chi_-|H|\chi_-\rangle - \langle\chi_+|H|\chi_+\rangle = \frac{(N+1)\,(\cos\theta_0)^2\,(\sin\theta_0)^N}{4\,[1-(\sin\theta_0)^{2N}]} \geqslant 0 \qquad (10)$$

justifies observation **(iii)**. Expression (10) has already been reported in [5]. One can probe through (7) that $\Delta_{\rm app} = 0$ at $h = 0$ for all N, and $\Delta_{\rm app}$ exponentially decays to zero as $N \to \infty$ due to the factor $(\sin\theta_0)^N$ for all $2h < 1$ [82]. The exact energy gap follows the power-law, viz. $\Delta := e_1 - e_0 \sim j^{-\frac{1}{3}}$ at the phase transition point $2h = 1$ [7, 8, 82], which we can not get from (10) because $\lim_{\theta_0 \to \frac{\pi}{2}} \Delta_{\rm app} = \frac{1}{4}$ for $N \gg 1$.

Before moving to the paramagnetic case, $1 \leqslant 2h$, let us record that $\mathcal{S} = \mathcal{E}_+ \oplus \mathcal{E}_-$ [for $\mathcal{S}$, see (3)]. Furthermore, taking the eigenkets of J_x, we can write

$$\mathcal{E}_+ = \text{span}\left\{\,|j-2k\rangle_x \mid k = 0, 1, \cdots, \lceil j - \tfrac{1}{2}\rceil\right\}, \qquad (11)$$
$$\mathcal{E}_- = \text{span}\left\{\,|j-(2k+1)\rangle_x \mid k = 0, 1, \cdots, \lfloor j - \tfrac{1}{2}\rfloor\right\},$$

where $\lceil\ \rceil$ and $\lfloor\ \rfloor$ are the ceiling and floor functions. One can differentiate the eigenkets of J_z in (3) from the eigenkets of J_x in (11) by their subscripts. For all $h > 0$, we obtain the exact eigenvalues $e_{0,1}$ and eigenkets $|e_{0,1}\rangle$ by restricting Hamiltonian (4) onto its invariant subspaces $\mathcal{E}_{+,-}$, respectively. In this way, we do not have to worry about the exponentially small gap Δ in the ferromagnetic phase.

Now we pick the paramagnetic case, where the mean-field ket $|\frac{\pi}{2}\rangle = |j\rangle_x \in \mathcal{E}_+$ as per (7) and (11). Comparing with (5), when $k < \infty$, every $|j-k\rangle_x$ gives the same minimum energy $\lim_{j\to\infty} \frac{{}_x\langle j-k|H|j-k\rangle_x}{j} = -h$ in the thermodynamic limit. So, for $1 \leqslant 2h$,

$$|\chi_0\rangle := \cos\tfrac{\mu_0}{2}\,|j\rangle_x + \sin\tfrac{\mu_0}{2}\,|j-2\rangle_x \in \mathcal{E}_+ \quad \text{and}$$
$$|\chi_1\rangle := \cos\tfrac{\mu_1}{2}\,|j-1\rangle_x + \sin\tfrac{\mu_1}{2}\,|j-3\rangle_x \in \mathcal{E}_- \qquad (12)$$

could be better approximations of $|e_0\rangle$ and $|e_1\rangle$, respectively, where $\mu_{0,1}$ provide the minimum energies $\varepsilon_{0,1} := \langle\chi_{0,1}|H|\chi_{0,1}\rangle$ over the two-dimensional subspaces of $\mathcal{E}_{+,-}$ where $|\chi_{0,1}\rangle$ live. In Appendix B, we obtain $\mu_{0,1}$ as well as $\varepsilon_{0,1}$ as functions of the field strength and the system size [see (B3) and (B4)]. In the thermodynamic limit, $\mu_{0,1}$ become

$$\mu_0 = \arccos\left(\frac{4h-1}{\sqrt{(4h-1)^2+\frac{1}{2}}}\right),$$
$$\mu_1 = \arccos\left(\frac{4h-1}{\sqrt{(4h-1)^2+\frac{3}{2}}}\right), \quad \text{and} \qquad (13)$$
$$\varepsilon_1 - \varepsilon_0 = h - \tfrac{1}{4} \quad \text{for a large } h$$

[see (B5)].

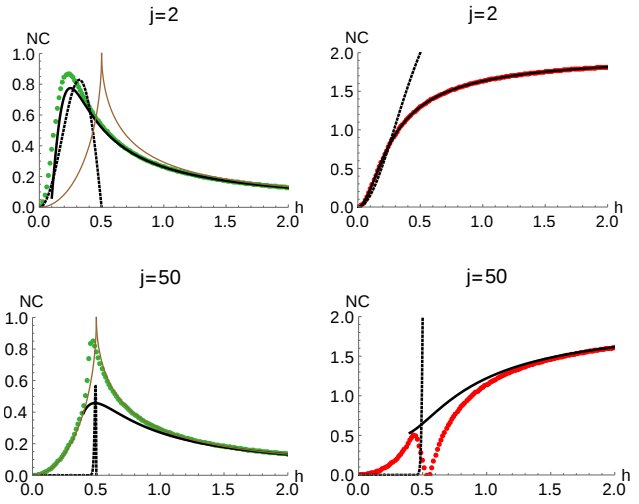

FIG. 4. Rescaled concurrence versus field strength. All the pictures show the rescaled concurrence $N\mathsf{C}$ for two different system sizes $N = 2j = 4, 100$. The green and red points on the left- and right-hand sides depict the rescaled concurrences for the exact ground $|e_0\rangle$ and first excited $|e_1\rangle$ state-vectors, respectively. The black dotted and continuous curves represent $N\mathsf{C}$ [from (16), (C10), and (C12)] for $|\chi_{+,-}\rangle$ and $|\chi_{0,1}\rangle$, respectively. The brown curves illustrate the rescaled concurrence $1-\sqrt{1-(2h)^2}$ for $0 \leqslant 2h \leqslant 1$ and $1-\sqrt{1-(2h)^{-1}}$ for $1 \leqslant 2h$ given in [30] for $|e_0\rangle$ in the thermodynamic limit. The green points follow the brown curve when j is large. On the other hand, C_e matches well with C_χ for almost all h when j is small and for $1 \leqslant h$ when j is large. In fact, for $j = 2$, $|e_1\rangle = |\chi_1\rangle$ for all $0 < h$. Whereas $|e_0\rangle$ deviates a bit from $|\chi_0\rangle$ as $|e_0\rangle$ lives in a larger space by one dimension.

In Fig. 1, for $h = 0.5, 0.7$, we display the overlaps $|\langle\chi_{0,1}|e_{0,1}\rangle|^2$, $\mu_{0,1}$, and the energy difference $\varepsilon_1 - \varepsilon_0$. There one can perceive that $\mu_0 \neq 0$ for both the h-values, hence $|\chi_0\rangle$ is a better approximation of the ground state-vector than the mean-field ket $|j\rangle_x$ for a finite j. One can further improve the approximation by adding more terms (that is, real multiples of $|j-4\rangle_x, |j-6\rangle_x, \cdots$) in the linear combination defined for $|\chi_0\rangle$ in (12) [for a method, see the text around (B2)]. For $j \gg 1$, even better approximation of the paramagnetic ground state is presented in [32].

On the right-hand side in Fig. 2, we present the values of $|\langle\chi_{0,1}|e_{0,1}\rangle|^2$, $\mu_{0,1}$, and $\varepsilon_1 - \varepsilon_0$ as functions of the field strength. One can witness that both $\mu_{0,1}$ decrease as h rises beyond the transition point. When the field strength is very large then obviously $|e_k\rangle \approx |j-k\rangle_x$ for $k = 0, 1, \cdots$. This implies $\mu_{0,1} \approx 0$ and $\varepsilon_1 - \varepsilon_0 \approx h - \frac{1}{4}$ in the thermodynamic limit, which is suggested in (13). In Fig. 3, we display the actual energy gap Δ, our results in black curves, and a result—$\sqrt{h(h-1/2)}$ for $1 \leqslant 2h$—from [8], which is exact for the limit $j \to \infty$. One can see that $\sqrt{h(h-1/2)} \approx h - \frac{1}{4}$ for a large h.

From Figs. 1, 2, and 18, we learned that the overlaps $|\langle\chi|e\rangle|^2$ are not close to one around the phase transition point. So our approximations $|e\rangle \approx |\chi\rangle$ does not work there, but as we move a bit away from $2h = 1$ they work reasonably well. The approximate energy gap—Δ_{app} for $2h < 1$ and $\varepsilon_1 - \varepsilon_0$ for $1 \leqslant 2h$—also matches well with the actual Δ for all h except in a small interval around the transition point [see Fig. 3].

Based on the above analysis, we assert that

$$|e_0\rangle \approx \left\{ \begin{matrix} |\chi_+\rangle \text{ for } 0 < h < \frac{1}{2} - \delta \text{ while } |\chi_-\rangle \\ |\chi_0\rangle \text{ for } \frac{1}{2} + \delta < h \qquad \text{while } |\chi_1\rangle \end{matrix} \right\} \approx |e_1\rangle , \tag{14}$$

where we put a small number $\delta > 0$ to exclude h-values near the critical point. This is our first result of the section.

In the remainder of this section, we shall compare the entanglement properties of $|e\rangle$ and of its approximation $|\chi\rangle$. Since both the mean field kets $|\theta_0\rangle$ and $|\pi - \theta_0\rangle$ are product state-vectors [see (A1)], they do not provide any information about the quantum entanglement of $|e\rangle$, but the kets $|\chi\rangle$ do. The concurrence C measures two-body entanglement, and it is introduced in [11, 12] as

$$\mathsf{C} = \max\left\{0\,,\, \sqrt{\lambda_{\text{m}}} - \sum_{\lambda \neq \lambda_{\text{m}}} \sqrt{\lambda}\right\}, \tag{15}$$

where $\lambda \geqslant 0$ are the eigenvalues of $\rho\,\widetilde{\rho}$, and $\lambda_{\text{m}} = \max\{\lambda\}$. The two-body 4×4 density matrix ρ is obtained here from a N-body quantum state by taking trace over all spins except the two between which we are measuring the entanglement, and $\widetilde{\rho} = (\sigma^y \otimes \sigma^y)\rho^*(\sigma^y \otimes \sigma^y)$, where ρ^* is the complex conjugate of ρ. Since our N-body states $|e\rangle\langle e|$ and $|\chi\rangle\langle\chi|$ are symmetric under the permutations of spins, ρ will be the same for each pair of spins.

We have numerically computed the concurrence of $|e_{0,1}\rangle$ by exploiting a result (C1) from [86] and presented it in Fig. 4. In Appendix C, we work out analytical formulas of the concurrence for $|\chi_\pm\rangle$ as well as $|\chi_{0,1}\rangle$, and they are

$$\begin{aligned} \mathsf{C}_{\chi_\pm} &= \frac{(\cos\theta_0)^2(\sin\theta_0)^{N-2}}{1 \pm (\sin\theta_0)^N}\,, \\ N\mathsf{C}_{\chi_0} &= \sqrt{2}\,\sin\mu_0 + 2\cos\mu_0 - 2 \quad \text{for } N \gg 1\,, \\ \lim_{N\to\infty}(N\mathsf{C}_{\chi_0}) &= \frac{(8h-1)}{\sqrt{(4h-1)^2 + \frac{1}{2}}} - 2\,, \\ N\mathsf{C}_{\chi_1} &= 4 - 2\,(\cos\mu_1 + \sqrt{6}\sin\tfrac{\mu_1}{2}) \quad \text{for } N \gg 1\,, \\ \lim_{N\to\infty}(N\mathsf{C}_{\chi_1}) &= 4 - 2\left(\frac{(4h-1)}{\sqrt{(4h-1)^2+\frac{3}{2}}} + \sqrt{3}\,\sqrt{1 - \frac{(4h-1)}{\sqrt{(4h-1)^2+\frac{3}{2}}}}\right). \end{aligned} \tag{16}$$

Taking θ_0 from (7), we have $\mathsf{C}_{\chi_\pm}$ as functions of the system size N and the field strength $h \in [0, \frac{1}{2})$. $\mathsf{C}_{\chi_\pm}$ decay exponentially with N due to the factor $(\sin\theta_0)^{N-2}$, however both show sharp peaks near the phase transition point when N is large [see Fig. 4]. Moreover, the peak $\lim_{h\to 1/2}(\mathsf{C}_{\chi_-}) = \frac{2}{N}$ decreases with N. Since every spin is interacting with all the others, the two-body entanglement gets diluted (due to the monogamy of entanglement

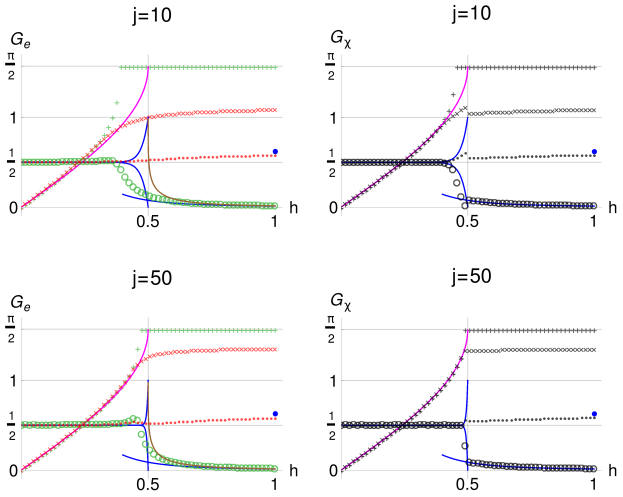

FIG. 5. Geometric entanglement versus field strength. In the left and right column, we display the geometric entanglement for the exact and approximate eigenstates, respectively. There is a good match between the left and right pictures except near the phase transition point $2h = 1$. The green (black) circles and red (black) dots depict G_e (G_χ) of $|e_0\rangle$ ($|\chi_{+\,\mathrm{or}\,0}\rangle$) and $|e_1\rangle$ ($|\chi_{-\,\mathrm{or}\,1}\rangle$), respectively. The three blue curves illustrate G of (18) and (19). Recall that the approximate eigenstate are from (8) for $2h < 1$ and (12) for $1 \leqslant 2h$. A green (black) "+" mark shows the value of ϑ where $|\langle\vartheta|e_0\rangle|^2$ ($|\langle\vartheta|\chi_{+\,\mathrm{or}\,0}\rangle|^2$) reaches its maximum value. The plus-marks closely follow the magenta curve—that highlights $\theta_0 = \arcsin(2h)$—in the range $h \in [0, \frac{1}{2}]$ and follow $\frac{\pi}{2}$ when $1 \leqslant 2h$. A green (black) "×" indicates ϑ where $|\langle\vartheta|e_1\rangle|^2$ ($|\langle\vartheta|\chi_{-\,\mathrm{or}\,1}\rangle|^2$) attains its highest value. The cross-marks also follow the magenta curve near the phase transition point, and then they deviate and saturate to a value. The saturated value changes with j. In the left-plots, the brown curve exhibits $1 - \sqrt{1 - (\sqrt{2h} - \sqrt{2h-1})^4}$, which is derived from Eqs. (4)–(6) in [32] for $1 \leqslant 2h$ and $j \gg 1$.

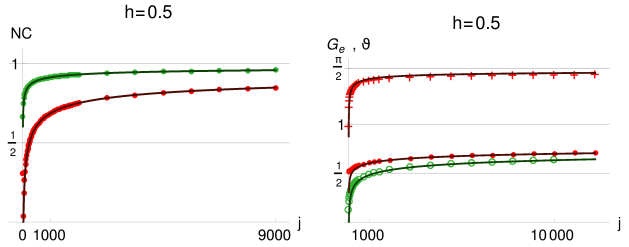

FIG. 6. Concurrence and geometric entanglement versus system size at the equilibrium phase transition point. At the phase transition point $2h = 1$, the exact rescaled concurrence $N\mathsf{C}$ and geometric entanglement G are displayed in the left and right panels, respectively. Like Figs. 4 and 5, the green and red color objects are associated with $|e_0\rangle$ and $|e_1\rangle$, respectively. A red +-marks represent the value of ϑ which gives the maximum overlap $|\langle\vartheta|e_1\rangle|^2$. The curves fitted the data-sets are described in the text around (21).

[84, 85]), hence the rescaled concurrence $N\mathsf{C}$ will provide the nontrivial information about the two-body entanglement [28]. So, in Fig. 4, all the plots display $N\mathsf{C}$.

Putting $\mu_{0,1}$ from (B3) and (B4) in (16), we gain the concurrences $\mathsf{C}_{\chi_{0,1}}$ as the functions of N and h. And, the thermodynamic limit of the concurrences are reached by having $\mu_{0,1}$ from (13). Note that the formula of C_{χ_0} in (16) holds for $h \geqslant \frac{5}{16} \approx 0.32$ (whereas, for all $h \geqslant 0$, it is given in (C10)). The concurrences of $|e\rangle$ and its approximation $|\chi\rangle$ matches well when either j is small or in the paramagnetic phase away from the transition point [see Fig. 4].

Next we consider the geometric measure of entanglement [13–27], which for a pure state $|\chi\rangle\langle\chi|$ is given by

$$\mathsf{G}_\chi := 1 - \max_{|\vartheta\rangle\langle\vartheta|} |\langle\vartheta|\chi\rangle|^2 \,, \tag{17}$$

where the maximum is taken over all the product states $|\vartheta\rangle\langle\vartheta| := \otimes_{i=1}^N |\vartheta_i\rangle\langle\vartheta_i|$. Since both exact $|e\rangle$ as well as approximate $|\chi\rangle$ eigenkets are symmetric under the particle-permutations and have real expansion coefficients in the basis $\mathcal{B}_z$ of (3), their closest product states will also follow these two properties. So, from (6) and (A1), we take the coherent ket $|\vartheta, \phi = 0\rangle \equiv |\vartheta\rangle$ with the angular variable $\vartheta \in [0, 2\pi)$ that covers all the real symmetric product kets of N spins.

The inner product $\langle\vartheta|\chi\rangle$ is given in (D1), and $|\langle\vartheta|\chi\rangle|^2$ versus ϑ plots are shown in Fig. 19. In the figure, for $2h < 1$, one can see that the maximum of $|\langle\vartheta|\chi_+\rangle|^2$ shifts from $\vartheta = \frac{\pi}{2}$ to $\vartheta = \theta_0$ and $\vartheta = \pi - \theta_0$ as j grows. On the other hand, $|\langle\vartheta|\chi_-\rangle|^2$ has two peaks of the equal height, and they move from 0 and π to θ_0 and $\pi - \theta_0$, respectively, as the system size increases. So, the maximum-values will be $|\langle\theta_0|\chi_\pm\rangle|^2$ for a large j, and thus we have

$$\mathsf{G}_{\chi_\pm} = \frac{1}{2}\left(1 \mp (2h)^N\right) \quad \text{for} \quad N \gg 1 \,. \tag{18}$$

Closer we are to the phase transition point $2h = 1$, larger N we need to achieve (18).

In the case of $1 \leqslant 2h$, the peak of $|\langle\vartheta|\chi_0\rangle|^2$ is always at $\vartheta = \frac{\pi}{2}$ [Fig. 19], so we get

$$\mathsf{G}_{\chi_0} = 1 - \left(\cos\frac{\mu_0}{2}\right)^2 \tag{19}$$

using (17) and (D1). Whereas $|\langle\vartheta|\chi_1\rangle|^2$ has two peaks of the same height, and they move from 0 and π towards $\frac{\pi}{2}$ as j grows, but we have to find ϑ numerically where the maximum of $|\langle\vartheta|\chi_1\rangle|^2$ occurs.

We numerically found the maxima of $|\langle\vartheta|e\rangle|^2$ and $|\langle\vartheta|\chi\rangle|^2$ and the values of ϑ where they occur. Then G_e and G_χ with the ϑ-values are presented in Fig. 5. One can observe a good match between G_e and the corresponding G_χ for all $j \geqslant 10$ and $h \geqslant 0$ except neat the phase transition point. Both $\mathsf{G}_{e_{0,1}}$ stay close to $\frac{1}{2}$ in the ferromagnetic phase, and G_{e_0} drops to zero while G_{e_1} becomes slightly more than one half in the paramagnetic phase. In fact, when $h \to \infty$, both $|e_1\rangle$ and $|\chi_1\rangle$ turn in to the w-ket

$|j-1\rangle_x$, whose geometric entanglement is given by [17]

$$\mathsf{G}_{\chi_1} = 1 - \left(\frac{N-1}{N}\right)^{N-1} \approx 1 - \frac{1}{\mathrm{e}} \quad \text{for} \quad N \gg 1\,. \tag{20}$$

The above value of G_{χ_1} is indicated by the blue point at $h = 1$ in Fig. 5. In the FCIM, it is interesting to see the first excited state as a GHZ-state [87] at one end of $0 < h < \infty$ and as a W-state [88] at the other end.

When the system size is large, the rescaled concurrence $N\mathsf{C}_e$ does not match with $N\mathsf{C}_\chi$ in the ferromagnetic phase [see Fig. 4]. Whereas the geometric entanglement G_e matches very well with G_χ for almost all h and j [see Fig. 5]. When $j \gg 1$, both $|\chi_\pm\rangle$ become similar to the GHZ-kets for almost all $h \in [0, \frac{1}{2})$ [5], and it is known that $\mathsf{C} = 0$ and $\mathsf{G} = \frac{1}{2}$ for a GHZ-ket [17, 86]. So it seems that as we increase h in the ferromagnetic phase the actual energy eigenkets $|e\rangle$ deviate from the GHZ-kets in such a way that $N\mathsf{C}_e$ become more than zero but G_e stays close to one half.

In Fig. 6, we present the rescaled concurrence $N\mathsf{C}_{e_{0,1}}$ and geometric entanglement $\mathsf{G}_{e_{0,1}}$ for both $|e_{0,1}\rangle$ at the critical point. The best-fitted functions in the figure suggest the large-j scalings

$$\begin{aligned} &1 - N\mathsf{C}_{e_{0,1}} \sim j^{-\frac{1}{3}}\,, \qquad 1 - \mathsf{G}_{e_0} \sim j^{-\frac{1}{6}}\,, \\ &1 - \mathsf{G}_{e_1} \sim j^{-0.12}\,, \quad \text{and} \quad \tfrac{\pi}{2} - \vartheta \sim j^{-0.35} \end{aligned} \tag{21}$$

in the case of $|e_1\rangle$. We want to emphasize that the numbers 0.12 and 0.35 are the estimated scalings based only on the numerical data in Fig. 6. Whereas for the ground state, the results in (21) are known [28–30, 32]. Also note that the geometric entanglement is defined differently in [32] than (17). In the case of $|e_1\rangle$, it is interesting to see that $\mathsf{G}_{e_1} \to 1$ at the critical point is captured by $\lim_{2h\to 1^-} \mathsf{G}_{\chi_-} = 1$ in (18).

III. TIME PERIOD AND CRITICAL TIMES IN THE QUENCH DYNAMICS

The dynamical phase transitions (DPTs) [9, 38–75], emerge in the evolution induced by a quantum quench, which is described as follows. Initially, the system is prepared in the ground state $|\psi_{\rm in}\rangle = |e_0\rangle$ of the Hamiltonian $H(h_{\rm in})$, where $h_{\rm in}$ is the initial field strength. At the time $t = 0$, we suddenly change the field magnitude from $h_{\rm in}$ to $h_{\rm f} \neq h_{\rm in}$, which begins the dynamics narrated by

$$|\psi(t)\rangle = \mathrm{e}^{-\mathrm{i}\,H_{\rm f}\,t}\,|\psi_{\rm in}\rangle\,, \tag{22}$$

where $H_{\rm f} := H(h_{\rm f})$. Since we are using a unit-free Hamiltonian, there is a constant factor having the unit of energy (precisely, Γ), that is kept silent in the exponential in the dynamical equation. There is also a factor of $1/\hbar$ that is kept silent in the same exponential. Together, they have made the time parameter t as unit-free. In other words, we have named the parameter $\Gamma/\hbar$ times time as t, which then is dimensionless.

Without loss of generality, we are taking both $h_{\rm in}, h_{\rm f} \geqslant 0$. Since H commutes with $\mathbf{S}^2$ [see (2)], the dynamics will be within the symmetric subspace (3), that is, $|\psi(t)\rangle \in \mathcal{S}$ for all the time and the total spin j remains conserved. Moreover, as we always stay in the subspace, we take $(\mathbf{S}, H) \equiv (\mathbf{J}, \widehat{H})$ [see (4)] in the following.

The DPT based on a dynamical order parameter, DPT-I, is studied in [9, 48, 51–57, 59, 70, 72, 74] for the FCIM. Usually, an order parameter is taken from the associated equilibrium phase transition. For example, in the case of $h_{\rm in} = 0$, the long-time average $\mathsf{m} := \lim_{\varsigma\to\infty} \int_0^\varsigma \mathsf{z}\,dt$ of the z-component of the mean vector

$$\begin{aligned} &\mathbf{s}(t) := \tfrac{1}{j}\langle\psi(t)|\mathbf{J}|\psi(t)\rangle = \mathbf{s}_{\rm cl}(t) + O\big(\tfrac{1}{j}\big)\,, \\ &\mathbf{s}_{\rm cl}(t) := (\sin\theta\cos\phi, \sin\theta\sin\phi, \cos\theta)\,, \end{aligned} \tag{23}$$

can be taken as a dynamical order parameter. As $h_{\rm f}$ increases, m goes from a nonzero value (ordered phase) to zero (disordered phase) at the dynamical phase transition point $h_{\rm f} = \frac{1}{4}$. In fact, when we quench from the ferromagnetic phase, $0 \leqslant 2h_{\rm in} < 1$, then the DPT-I occurs at $h_{\rm f} = \frac{1}{2}(h_{\rm in} \pm h^{\rm eq})$ [48, 52, 70, 72], which can be deduced from energy conservation (25). Recall that the equilibrium phase transition point $h^{\rm eq} = \frac{1}{2}$ in the FCIM.

Taking the Heisenberg equation of motion $\frac{d\mathbf{J}}{dt} = \mathrm{i}[H, \mathbf{J}]$ and then replacing $\frac{\mathbf{J}}{j}$ with $\mathbf{s}_{\rm cl}$ in the classical limit $j \to \infty$, one gets [9, 48, 74]

$$\begin{aligned} &\frac{d\theta}{dt} = h_{\rm f}\,\sin\phi \quad \text{and} \\ &\frac{d\phi}{dt} = -\frac{1}{2}\cos\theta + h_{\rm f}\,\cot\theta\,\cos\phi \end{aligned} \tag{24}$$

for the unit-vector $\mathbf{s}_{\rm cl}$ of (23). For a finite $N = 2j$, the classical equations of motion (24) quite accurately give the short-time evolution of the mean vector $\mathbf{s}(t)$ [for example, see Fig. 8]. After the quench, the energy remains conserved,

$$\mathscr{E}_{h_{\rm f}}\big(\theta(t), \phi(t)\big) = \mathscr{E}_{h_{\rm f}}(\theta_{\rm in}, \phi_{\rm in})\,, \tag{25}$$

for all the time $t \geqslant 0$ [for $\mathscr{E}$, see (5)]. The initial values $(\theta_{\rm in}, \phi_{\rm in})$ are fixed by $h = h_{\rm in}$ as per (7) and (25).

The so-called DPT-II is based on the Loschmidt rate function [60, 75]

$$\begin{aligned} &r_\infty(t) := \lim_{N\to\infty} r(t)\,, \quad \text{where} \\ &r(t) := \frac{1}{N}\ln\left(\frac{1}{p(t)}\right)\,, \\ &p(t) := |\langle\psi_{\rm in}|\psi(t)\rangle|^2 = \Big|\sum_k \mathrm{e}^{-\mathrm{i}\,E_k t}|\langle\psi_{\rm in}|E_k\rangle|^2\Big|^2 \end{aligned} \tag{26}$$

is the probability (known as the Loschmidt echo) of returning to the initial state, and E_k and $|E_k\rangle$ are the energy eigenvalues and eigenkets of the final Hamiltonian $H_{\rm f}$. We associate the eigenenergies e and E with $H_{\rm in}$ and $H_{\rm f}$, respectively.

In the case of DPT-II, there is no time-averaging, and the time when kinks appear in $r(t)$ are called the critical times for fixed $h_{\rm in}$ and $h_{\rm f}$. The rate function $r_\infty(t)$ is a dynamical counterpart of the free energy density [60, 75], and a kink or cusp represents a sharp change in its first derivative with respect to time. By keeping $h_{\rm in}$ fixed, one can alternatively investigate how $r_\infty(t)$ as a whole, that is for all $t \geqslant 0$, changes as a function $h_{\rm f}$. Then, one can define different phases with respect to $h_{\rm f}$. In Secs. III A and III B, we consider $h_{\rm in} = 0$ (quench from the ferromagnetic phase) and $h_{\rm in} \to \infty$ (quench from the paramagnetic phase) separately.

In the case of $h_{\rm in} = 0$, the two DPT-II phases—the anomalous phase when $h_{\rm f} \in (0, \frac{1}{4})$ and the regular phase when $h_{\rm f} > \frac{1}{4}$—of the FCIM are discovered in [69, 70]. There it is also shown that, in the case of $h_{\rm in} \to \infty$, the two DPT-II phases will be the regular phase when $h_{\rm f} \in [0, \frac{1}{2}]$ and the trivial phase when $h_{\rm f} > \frac{1}{2}$. In the trivial phase, $r_\infty(t)$ has no cusp, whereas both the regular and anomalous phases have infinite sequences of cusps. In the regular and anomalous phases the first cusp appears before and after the first minimum of $r_\infty(t)$, respectively. The DPT-II is investigated in [52, 57, 59, 69–74] for the FCIM.

A. Initially all spins are up in z-direction

Throughout this subsection, we fix $h_{\rm in} = 0$. Hence, for every N, the Hamiltonian has two minimum energy eigenkets $|\pm j\rangle_z$, out of which we choose $|\psi_{\rm in}\rangle = |+j\rangle_z$. It means, initially, all the spins are up in the z-direction and $\theta_{\rm in} = 0$.

1. *DPT-I*

Let us first consider the DPT-I. Here the energy conservation (25) becomes

$$\sin\theta = (4h_{\rm f})\,\cos\phi\,, \tag{27}$$

which determines $\phi_{\rm in} = \frac{\pi}{2}$ as per $h_{\rm f} > 0$. Before moving ahead we want to emphasize that, up to a large extent, the results between (27) and (33) have known through [9, 48, 51–54, 70], and similar calculations are reported for other mean-field models [43–45, 47, 49, 50]. In this subsection, our main results are in Table I, the bottom-right plot in Fig. 7, (35), and (36). They basically show how the time period denoted by T varies with the system size for different $h_{\rm f}$.

By taking the top and bottom equations of (24) for $1 < 4h_{\rm f}$ and $4h_{\rm f} < 1$, separately, one can reach their solutions

$$\begin{aligned} F\left(\theta\,|\,(4h_{\rm f})^{-2}\right) &= h_{\rm f}\,t \quad \text{for} \quad 1 < 4h_{\rm f} \quad \text{and} \\ F\left(\tfrac{\pi}{2} - \phi\,|\,(4h_{\rm f})^{2}\right) &= \tfrac{1}{4}\,t \quad \text{for} \quad 4h_{\rm f} < 1 \end{aligned} \tag{28}$$

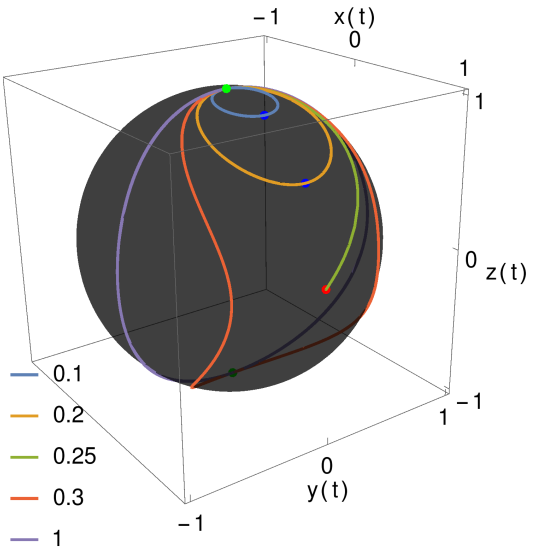

FIG. 7. Classical trajectories on the unit sphere. Trajectories of $\mathbf{s}_{\rm cl} = (\mathsf{x}, \mathsf{y}, \mathsf{z})$ [defined in (23)] are highlighted in separate colors—on the black unit sphere—for different magnitudes of $h_{\rm f} = 0.1, \cdots, 1$. Such trajectories are theoretically and experimentally obtained in [53, 55–57, 59, 72, 73]. Individual components of $\mathbf{s}_{\rm cl}$ are shown by the dotted curves in Fig. 8. All the paths start from the green point $(0, 0, 1)$ towards the positive y-direction, that is, $(\theta_{\rm in}, \phi_{\rm in}) = (0, \frac{\pi}{2})$. The blue points $(4h_{\rm f}, 0, \sqrt{1-(4h_{\rm f})^2})$ are the turning points for $h_{\rm f} < \frac{1}{4}$. Whereas, the green point $(0, 0, -1)$ is the turning point for all $\frac{1}{4} < h_{\rm f}$. From the starting to the turning point, $\mathbf{s}_{\rm cl}$ takes the time $T_{\rm cl}/2$, where the time period $T_{\rm cl}$ depends on $h_{\rm f}$ as per (32). In the case of $h_{\rm f} = \frac{1}{4}$, $\mathbf{s}_{\rm cl}$ takes infinite time to reach the red point $(1, 0, 0)$, and thus it never returns [see also Fig. 8].

with the help of (27), where

$$\begin{aligned} F(\gamma\,|k^2) &:= \int_0^\gamma \frac{dw}{\sqrt{1-(k\,\sin w)^2}} \quad \text{and} \\ K(k^2) &:= F(\tfrac{\pi}{2}|k^2) \end{aligned} \tag{29}$$

are the incomplete and complete elliptic integrals of the first kind. The inverse of F is the Jacobian amplitude 'am', and thus we gain [52]

$$\begin{aligned} \theta &= \text{am}\left(h_{\rm f}\,t\,|\,(4h_{\rm f})^{-2}\right) \quad \text{for} \quad 1 < 4h_{\rm f} \quad \text{and} \\ \phi &= \tfrac{\pi}{2} - \text{am}\left(\tfrac{1}{4}\,t\,|\,(4h_{\rm f})^{2}\right) \quad \text{for} \quad 4h_{\rm f} < 1\,. \end{aligned} \tag{30}$$

Once we have one of the angles then the other one comes from (27). In the case of $4h_{\rm f} = 1$, one can directly get

$$\theta = -\tfrac{\pi}{2} + 2\arctan(\mathrm{e}^{\frac{t}{4}}) = \tfrac{\pi}{2} - \phi \tag{31}$$

from (24) by exploiting (27).

By putting the angles from (30) and (31) in (23), we draw the trajectories of $\mathbf{s}_{\rm cl}(t)$ for different $h_{\rm f}$ in Fig. 7. All these trajectories obey energy conservation (27). The

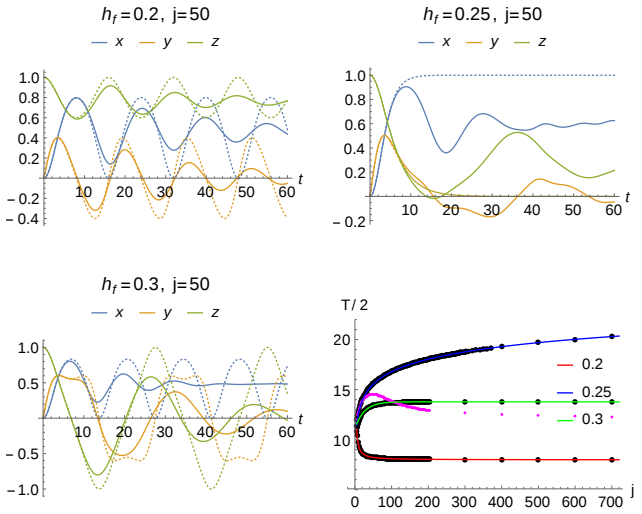

FIG. 8. Spin components versus time and the half time period versus system size. In the first three panels, we display the components of $\mathbf{s} = (\mathsf{x}, \mathsf{y}, \mathsf{z})$ with the solid and of $\mathbf{s}_{\rm cl}$ with the dotted curves for $h_{\rm f} = 0.2, 0.25$, and 0.3. The mean vector $\mathbf{s}$ is computed numerically for $j = 50$, and $\mathbf{s}_{\rm cl}$ is acquired from (23), (30), and (31). The amplitude of oscillations does not change with time t in the dotted curves that correspond to the classical trajectories in Fig. 7. In the bottom-right plot, for $h_{\rm f} = 0.2, 0.25$, and 0.3, $\frac{T}{2}$ for different j-values are represented by the black points. A curve passing through a sequence of black points depicts the associated best fit function $\mathsf{g}(j)$ listed in Table I. The dots in magenta color show $\frac{T}{2}$ for $h_{\rm f} = 0.245$.

vector $\mathbf{s}_{\rm cl}(t)$ takes the half time period from the starting point $(0, 0, 1)$ to the turning point, where θ goes from 0 to π in the case of $1 < 4h_{\rm f}$ and ϕ goes from $\frac{\pi}{2}$ to 0 in the case of $4h_{\rm f} < 1$. Hence, using (28) and (29), one can express the time period $T_{\rm cl}$ and the order parameter $\mathsf{m}_{\rm cl} := \frac{1}{T_{\rm cl}} \int_0^{T_{\rm cl}} \mathsf{z} dt$ as [48, 70]

$$T_{\rm cl} = \begin{cases} \frac{4}{h_{\rm f}} K\big((4h_{\rm f})^{-2}\big) & \text{for } \ 1 < 4h_{\rm f} \\ 8\, K\big((4h_{\rm f})^{2}\big) & \text{for } \ 4h_{\rm f} < 1 \end{cases} \quad \text{and}$$

$$\mathsf{m}_{\rm cl} = \begin{cases} 0 & \text{for } \ 1 < 4h_{\rm f} \\ \frac{4\pi}{T_{\rm cl}} & \text{for } \ 4h_{\rm f} < 1 \end{cases} . \tag{32}$$

To get $\mathsf{m}_{\rm cl}$ in (32), one needs to realize that $\int_0^{T_{\rm cl}} \cos\theta\, dt$ is

$$\frac{1}{h_{\rm f}} \int_0^0 \frac{\cos\theta\, d\theta}{\sqrt{1 - \big(\frac{\sin\theta}{4h_{\rm f}}\big)^2}} = 0 \quad \text{and} \quad -4 \int_{\frac{\pi}{2}}^{-\frac{\pi}{2}} d\phi = 4\pi \tag{33}$$

when $1 < 4h_{\rm f}$ and $4h_{\rm f} < 1$, correspondingly. One can derive (33) from (24) with the help of (27). In the case of $4h_{\rm f} = 1$, we have $\int_0^{T_{\rm cl}} \cos\theta\, dt = \int_0^{\infty} \frac{1}{\cosh(t/4)}\, dt = 2\pi$ from (31), and thus $\mathsf{m}_{\rm cl} = 0$. The plots for $T_{\rm cl}$ and $\mathsf{m}_{\rm cl}$ are given in [53, 70] and Fig. 10.

Taking the dynamical order parameter $\mathsf{m}_{\rm cl}$, the DPT-I is described in [48, 52, 70, 72]: for $h_{\rm in} = 0$, the dynamical

TABLE I. The best fit functions for the half time period. For $h_{\rm in} = 0$, the best fit functions $\mathsf{g}(j)$ for $\{\frac{T_j}{2}\}$ are recorded here with their MSE (minimum mean square error) defined in Appendix E. The time period $T_{\rm cl}$ comes from (32). Both the g-functions for $h_{\rm f} = 0.3$ deliver almost the same plot in Fig. 8.

$h_{\rm f}$	$\frac{T_{\rm cl}}{2}$	$\mathsf{g}(j)$	MSE
0.2	7.98121	$\frac{T_{\rm cl}}{2} + 18.23\, j^{-1.1}$	0.0002
0.25	∞	$8.48102 + 1.80448\, \ln(j)$	0.0001846
0.3	13.7817	$\frac{T_{\rm cl}}{2} - 48.4304\, j^{-1.26}$	0.00293
		$\frac{T_{\rm cl}}{2} - 2.70305\, \mathrm{e}^{-0.04\, j}$	0.00176

ordered ($\mathsf{m}_{\rm cl} \neq 0$) and disordered ($\mathsf{m}_{\rm cl} = 0$) phases occur when $h_{\rm f} \in [0, \frac{1}{4})$ and $h_{\rm f} > \frac{1}{4}$, respectively. Hence, in the case of $h_{\rm in} = 0$, $h_{\rm f}^{\rm dy} = \frac{1}{4}$ is the *dynamical* critical point for the DPT-I and also for the DPT-II [52, 70, 72] that we will discuss in the next subsection.

Now we present our contribution for this subsection where we show how the exact time period T goes to $T_{\rm cl}$ as we increase the system size $N = 2j$. Unlike the classical vector $\mathbf{s}_{\rm cl}(t)$, motion of the exact quantum mean vector $\mathbf{s}(t)$ [defined in (23)] is not perfectly periodic when N is finite. In Fig. 8, we plot all the three components of $\mathbf{s}(t)$ as well as of $\mathbf{s}_{\rm cl}(t)$ for separate $h_{\rm f}$ by picking $j = 50$. There one can notice that $\mathbf{s}$ closely follows $\mathbf{s}_{\rm cl}$ in the beginning for a short time. The time interval over which the quantum evolution matches with its classical limit increases with N [53]. So, by looking at Figs. 7 and 8, we define the time $\frac{T}{2}$ when the z-component of $\mathbf{s}$ reaches its first minimum value. In this way, we numerically obtain $\frac{T}{2}$ for different j-values and exhibit the data in the bottom-right plot in Fig. 8. For the DPT-I, z versus t plots are studied in [52, 70, 72, 74].

By employing the least squares method from Appendix E, we get the best fit function $\mathsf{g}(j)$ for the data $\{\frac{T_j}{2}\}$ associated with $h_{\rm f}$. For distinct $h_{\rm f}$, the functions g are placed in Table I and exhibited in Fig. 8. The fitted functions reveal that T diverges logarithmically at the critical point $h_{\rm f} = \frac{1}{4}$ and converges to $T_{\rm cl}$ otherwise. In the table and figure, one can also notice that $\mathsf{g}(j)$ changes its behavior from a convex to a concave function as we increase $h_{\rm f}$. To visualize it clearly we also present $\frac{T}{2}$ as a function of j in the figure for $h_{\rm f} = 0.245$, where $\frac{T}{2}$ has both the convex and concave parts.

The time period T diverges when we take both the limits $j \to \infty$ and $4h_{\rm f} \to 1$. **Case 1:** One can take first $j \to \infty$. Then the time period will be $T_{\rm cl}$ of (32) and the left-hand limit

$$\lim_{4h_{\rm f} \to 1^-} K\left((4h_{\rm f})^2\right) = \lim_{4h_{\rm f} \to 1^-} \ln\left(\frac{4}{\sqrt{1 - (4h_{\rm f})^2}}\right) \tag{34}$$

reveals the log-divergence with respect to the Hamiltonian parameter like in the case of a simple pendulum as reported in [53, 54] and in other mean-field models [43–45, 47, 49, 50]. Equation (34) is borrowed from [89]. The

right-hand limit $4h_{\rm f} \to 1^+$ on $K((4h_{\rm f})^{-2})$ will deliver the same outcome. **Case 2:** One can fix first $4h_{\rm f} = 1$ and then compute the exact T for different system sizes and observe the log-divergence with respect to j as exhibited in Fig. 8 and Table I.

Now we demonstrate how one can take both the limits together. For all $0 \leqslant 4h_{\rm f} \leqslant 1$, the turning point is $(\sin\theta_{\rm tp}, 0, \cos\theta_{\rm tp}) = (4h_{\rm f}, 0, \sqrt{1-(4h_{\rm f})^2})$. Suppose we increase $h_{\rm f}$ and j by maintaining a relation, say, $\frac{1}{j^\kappa} = \frac{\pi}{2} - \theta_{\rm tp} =: \epsilon$, where $\kappa > 0$. Then, the limit $j \to \infty$ will also serve the purpose of $4h_{\rm f} \to 1^-$. Moreover, we gain

$$\lim_{4h_{\rm f}\to 1^-} \frac{T_{\rm cl}}{2} = \lim_{\epsilon\to 0} 4\ln\left(\frac{4}{\sin\epsilon}\right) = \lim_{j\to\infty} 4\kappa \ln j + 4\ln 4 \qquad (35)$$

by exploiting (32), (34), and $\sin\epsilon \approx \epsilon$. If we take $\epsilon := \frac{1}{\alpha j^\kappa}$ with $\alpha > 0$, then we can find out the values of κ and α for which $\frac{T_{\rm cl}}{2}$ of (35) matches with $\mathsf{g}(j)$ given in Table I for $4h_{\rm f} = 1$.

In fact, one can get an equation similar to the first one in (35) from (31) as follows. Taking the z-component of $\mathbf{s}_{\rm cl}$ as per (31), we have the quadratic equation $\cos\theta = \frac{2\varpi}{1+\varpi^2}$, where $\varpi = \exp(t/4)$. Solving this equation for ϖ and then for t provides

$$t = 4\ln\left(\frac{1+\sin\theta}{\cos\theta}\right) \approx 4\ln\left(\frac{2}{\sin\varepsilon}\right), \qquad (36)$$

where $\varepsilon := \frac{\pi}{2} - \theta \approx 0$ measure how close the associated point on the classical trajectory is from the destination point $(1,0,0)$, which is shown in red color in Fig. 7.

2. *DPT-II*

Now we consider the DPT-II. Let us recall that $h_{\rm in} = 0$, $|\psi_{\rm in}\rangle = |j\rangle_z \in \mathcal{S}$, $h_{\rm in} < h_{\rm f}$, and the Loschmidt rate function $r(t)$ from (26). In the FCIM, there will always be kinks in $r(t)$ at the so-called critical times [69, 70]. In the paper we only focus on the first critical time—when the *first* kink appears in $r(t)$—denoted by τ. In this subsection, our main results are presented in Table II and Figs. 10, 11, and 12. They essentially tell that, similar to T in the previous subsection, the sequence τ_j converges to a value when $4h_{\rm f} \neq 1$, and divergences logarithmically with the system size at the dynamical phase transition point $4h_{\rm f} = 1$.

Now let us begin with Fig. 9, where we display $r(t)$ for different $h_{\rm f}$, which are studied in [69–71, 73, 74] for the DPT-II. In Fig. 9 (a), one can observe that the first kinks—marked by the arrows—appear at the fourth, third, and second peaks of $r(t)$ when $h_{\rm f} = 0.1$, 0.115, and 0.145, respectively. It is also observed in [69, 71], which implies that τ decreases from ∞ to a value around 16 as $h_{\rm f}$ rises from 0 to 0.145 [see also Fig. 10]. For all $h_{\rm f} \in [0.145, \frac{1}{4}]$, the first kink emerges at the second peak

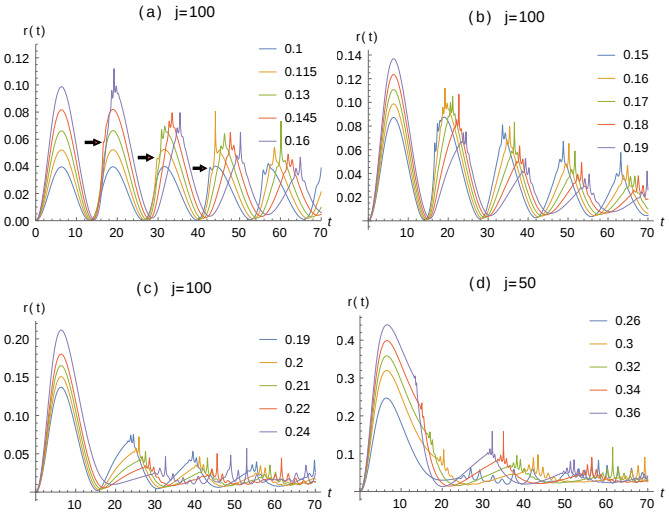

FIG. 9. The rate versus time. The Loschmidt rate $r(t)$ as a function of time is displayed here in different colors for $h_{\rm f} = 0.1, \cdots, 0.36$, where $h_{\rm in} = 0$ in all the plots. Each subfigure bears the value of j for which the plots are generated (for more such plots, see [52, 70, 72–74]).

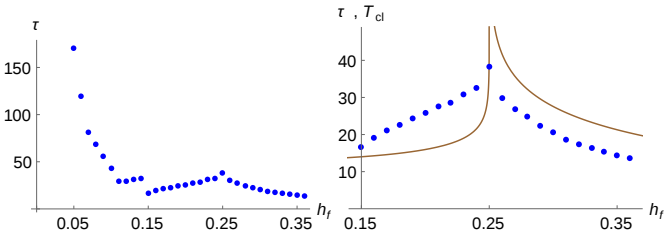

FIG. 10. First critical time versus final field strength. Taking $j = 100$, we plot the first critical time τ (blue points) with respect to the field's strength $h_{\rm f} = 0.05, \cdots, 0.36$. Experimentally, a similar plot is obtained in [59] for $1 < 4h_{\rm f}$. The right-plot is a part of the left-plot. For comparison, we place the brown curves that represent the classical time period given in (32).

as shown in Fig. 9(a)–(c). However, the kink moves at a later time as $h_{\rm f}$ grows. It reveals that τ rises from 16 as we increase the final field's strength from 0.145 to $\frac{1}{4}$. In Fig. 9(a)–(c), the system size is fixed, $j = 100$.

The height of peaks (roughly) grows with $h_{\rm f}$ until $h_{\rm f} \approx 0.16$, then except for the first peak the height decreases with the field's magnitude until $h_{\rm f} = \frac{1}{4}$. Except the first peak, all peaks are lost and replaced by rapid oscillations in $r(t)$ at the *dynamical* critical point $h_{\rm f}^{\rm dy} = \frac{1}{4}$. When we go beyond the critical point towards a higher $h_{\rm f}$ value, the kink occurs at the first peak [see Fig. 9(d)] and at an earlier time. It illustrates that τ decreases towards 0 as we increase $h_{\rm f}$ from $\frac{1}{4}$ to ∞. Moreover, in this range of $h_{\rm f}$, the height of peaks rises with the field's strength. In the case of $h_{\rm in} = 0$, the two phases of DPT-II are characterized by no kink (anomalous phase, when

$4h_{\rm f} < 1$) or a kink (regular phase, when $1 < 4h_{\rm f}$) on the first peak before the first minimum of $r(t)$ [69, 70].

By taking $\varsigma = 0.01$, we have numerically computed the derivative using

$$\dot{r} \approx \frac{-r(t+2\varsigma) + 8r(t+\varsigma) - 8r(t-\varsigma) + r(t-2\tau)}{12\varsigma} \quad (37)$$

on a set of points in an appropriate time interval and obtain τ where the absolute difference $|\dot{r}(t+\varsigma) - \dot{r}(t)|$ is maximum. Thus the obtained τ are plotted in Figs. 10, 11, 12, 16, and 17. The error in approximation (37) is $O(\varsigma^4)$.

In Fig. 10, we present τ versus $h_{\rm f}$ plot for a fixed system size. The plot summarizes the two paragraphs written above (37). When $h_{\rm f} = 0.05$ is close to $h_{\rm in} = 0$, the ground state $|\psi_{\rm in}\rangle$ does not change much for a long time, and hence the first cusp appears on the 14th peak of $r(t)$. When $h_{\rm f} = 0.06$, the cusp emerges on the 10th peak, which shows a rapid decline in τ with a small increase in $h_{\rm f}$. A small jump in τ around $h_{\rm f} = 0.15$ is because the first kink shifts from the 3rd to 2nd peak as $h_{\rm f}$ moves from 0.14 to 0.15. A similar shift happens around $h_{\rm f} = 0.1$ in Fig. 10. If we focus on $h_{\rm f} \in [0.15, 0.35]$ in the figure, then we observe τ and $T_{\rm cl}$ of (32) exhibit a similar behavior: both grow with $h_{\rm f}$, reach a peak at the dynamical phase transition point, and then they decrease.

Now we discuss how τ varies with j for a fixed $h_{\rm f}$. Let us take Fig. 11, where we present $r(t)$ and τ for different j and for $h_{\rm f} = 0.145, 0.16$ separately. In the case of $h_{\rm f} = 0.145$, one can observe a cusp at $r(t)$ gets sharper and sharper as j increases, and it gradually shifts towards the left-hand side. Consequently, one can see the sequence τ_j decreases monotonically and converges to a value around 16. Following the least squares method of Appendix E, we find the best fit function $\mathsf{g}(j)$ for the data $\{\tau_j\}$ and registered it in Table II. One can see that g is a convex function, it represents a power-law convergence of τ_j for $h_{\rm f} = 0.145$, where the estimates of τ_∞ and the finite-size scaling are 15.8235 and 0.75, respectively. These estimates are described in Appendix E.

Now we focus on $r(t)$ for $h_{\rm f} = 0.16$ in Fig. 11. As we change j, the position of cusp, that is, τ oscillates around some value, and the oscillations become smaller as j grows larger and larger. This manifests the convergence of τ_j. If we do not (or do) ignore a first set of values in the data $\{\tau_j\}$, then g turns out to be a convex (concave) function. Both the convex and concave functions for $h_{\rm f} = 0.16$ are placed in Table II and plotted in Fig. 11 with the data. Both the functions belong to the exponential-class, and they suggest the same $\tau_\infty \approx 19$ but their finite-size scalings are different. For $h_{\rm f} < 0.16$, g are mostly convex functions, and they all are concave functions for $h_{\rm f} > 0.16$. This change of behavior we also have observed in the case of time period T [see Fig. 8 and Table I]. By the way, we get similar plots if we replace $h_{\rm f} = 0.145$ ($h_{\rm f} = 0.16$) by $h_{\rm f} = 0.113$ ($h_{\rm f} = 0.14$).

One can see in Fig. 11 for $h_{\rm f} = 0.16$ that there are multiple spikes at $r(t)$ for each j, one of which is the sharpest

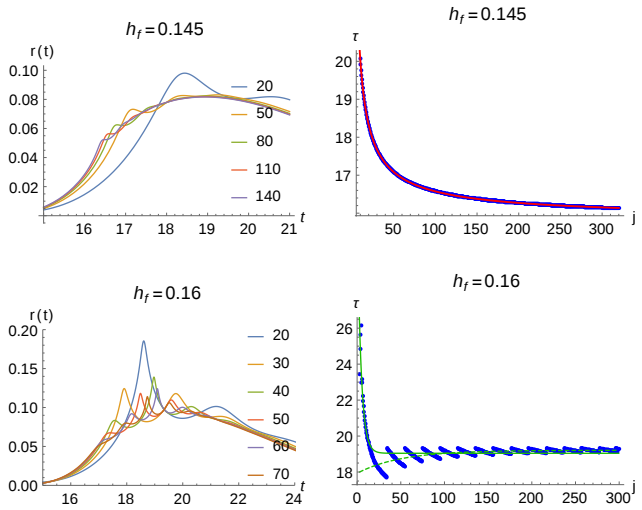

FIG. 11. The rate versus time and the first critical time versus system size. In all the plots $h_{\rm in} = 0$, and the value of $h_{\rm f}$ is written at the top of each picture. In the left-column, we present $r(t)$ in distinct colors for different j-values. In the right-column, the first critical times τ_j are depicted by the blue dots, and the red and green curves represent the best fit functions $\mathsf{g}(j)$ of the form $\mathsf{a} + \mathsf{b}\, j^{\mathsf{c}}$ (power-law) and $\mathsf{a} + \mathsf{b}\, \mathrm{e}^{\mathsf{c}\, j}$ (exponential), respectively. The continuous and dotted green curves express the corresponding convex and concave functions. All the g functions with their $h_{\rm f}$ are recorded in Table II.

measured by $|\dot{r}(t+\varsigma) - \dot{r}(t)|$. Recall that the time at the sharpest spike is our τ_j. For a sequence of j-values this particular spike—moves a bit on the left-hand side and—remains the sharpest, and then another spike becomes so. As a result, we see sudden jumps (oscillations) in τ_j in the case $h_{\rm f} \geqslant 0.16$ [see Fig. 12]. Due to the oscillations, the value of MSE is larger in the case of $h_{\rm f} = 0.16$ in comparison to $h_{\rm f} = 0.145$ [see Table II].

Now we move to Fig. 12 that is an extension of Fig. 11. There, in the case of $h_{\rm f} = 0.2, 0.3$, one can observe a convergent behavior of $r(t)$ [for more details, see Appendix F] and thus of τ with respect to j. There are oscillations in τ but they get suppressed as we increase the system size $N = 2j$. Whereas, at the dynamical phase transition point $h_{\rm f} = 0.25$, large and fast oscillations in $r(t)$ pertain for a long time, and thus it becomes difficult to assign τ. So, we pick the values $h_{\rm f} = 0.245, 0.255$ close to the transition point and obtain the data $\{\tau_j\}$. For each of these values, the best fit functions g are in Table. II that suggests the *logarithmic divergence* of τ_j with respect to j at the dynamical critical point. The same type of divergence we have reported for the time period T_j in the previous subsection. For $h_{\rm f} = 0.2, 0.3$, and 0.4, the best fit functions for the data $\{\tau_j\}$ are placed in Table. II and plotted in Fig. 12.

TABLE II. The best fit functions for the first critical time. For $h_{\rm in}=0$, the best fit functions $\mathsf{g}(j)$ for τ_j are recorded here with their MSE defined in Appendix E. In the case of $h_{\rm f}=0.2, 0.3$, two different functions have almost the same mean square error, so we put both of them in this table and exhibit them in Fig. 12 through red and green curves.

$h_{\rm f}$	$\mathsf{g}(j)$	MSE
0.05	$167.235+54.1995\,j^{-0.64}$	0.00136
0.095	$41.3729+29.1247\,j^{-0.69}$	0.0000274
0.145	$15.8235+23.727\,j^{-0.75}$	0.000022
0.16	$19.0431+13.626\,\mathrm{e}^{-0.23\,j}$	0.110756
	$19.209-1.27974\,\mathrm{e}^{-0.02\,j}$	0.0390285
0.2	$26.8408-16.7947\,j^{-0.577}$	0.0887059
	$26.2424-4.66818\,\mathrm{e}^{-0.026\,j}$	0.086753
0.245	$23.9705+2.14523\,\ln(j)$	0.395034
0.255	$17.9401+2.81186\,\ln(j)$	0.128846
0.3	$21.004-8.65749\,j^{-0.6}$	0.0521935
	$20.6731-3.00326\,\mathrm{e}^{-0.04\,j}$	0.0565792
0.4	$11.4106-2.93687\,\mathrm{e}^{-0.241\,j}$	0.123572

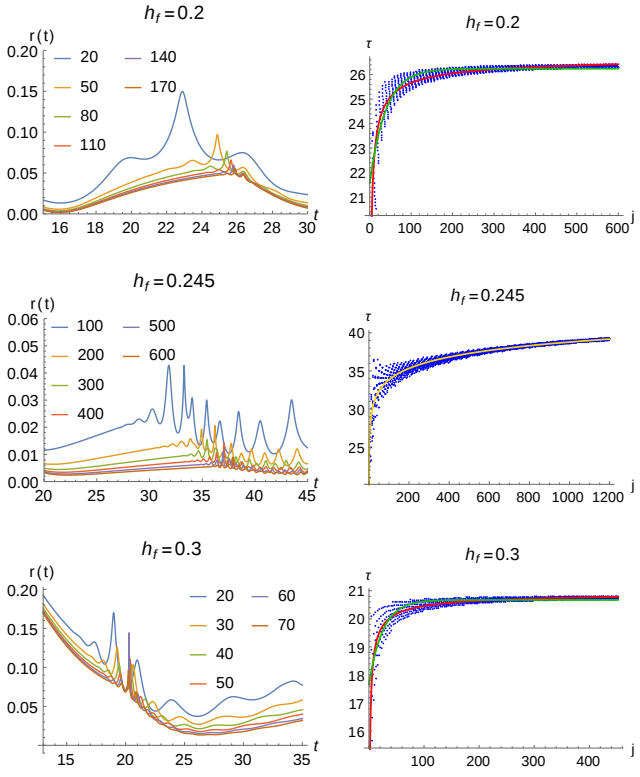

FIG. 12. The rate versus time and the first critical time versus system size. In the same fashion, this figure presents the items of Fig. 11 for the other values of $h_{\rm f}$. The fitted curve in yellow color stands for the logarithmic function given in Table II for $h_{\rm f}=0.245$. Like before, the red and green fitted curves represent functions from the power-law and exponential families.

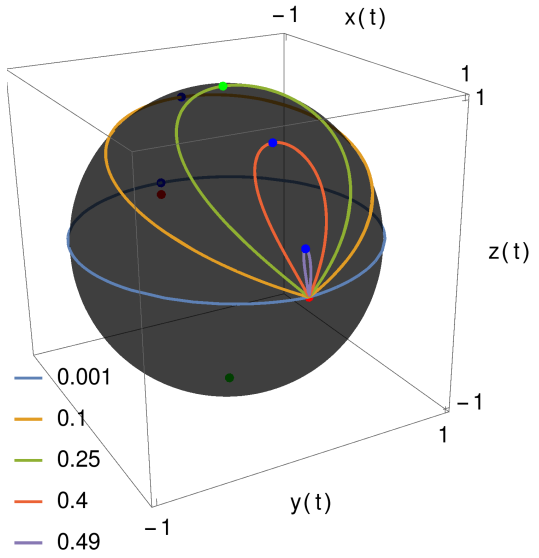

FIG. 13. Classical trajectories on the unit sphere. Trajectories of $\mathbf{s}_{\rm cl}$ are illustrated in different colors for $h_{\rm f}=0.001,\cdots,0.49$. They are obtained by numerically solving equations of motion (24) with the initial condition $(\theta_{\rm in},\phi_{\rm in})=(\frac{\pi}{2}-\epsilon,0)$, where $\epsilon=10^{-3}$. Since $\epsilon>0$, the motion will be on the upper hemisphere. Every trajectory starts from the red point—that is approximately $(1,0,0)$—towards the negative y-direction and follows energy conservation (38).

B. Initially all spins are up in x-direction

Throughout this subsection, we fix $h_{\rm in}\to\infty$, and thus $|\psi_{\rm in}\rangle=|\frac{\pi}{2},0\rangle=|j\rangle_x$ is the exact ground state of Hamiltonian (4) as per (7). Like Sec. III A, let us focus on the DPT-I and DPT-II sequentially.

1. *DPT-I*

A power-law divergence of the time period in (40), (41), Fig. 14, and Table III and a power-law decay of the dynamical order parameter in (43) are our main contributions in this subsection. Here the energy conservation (25) becomes

$$4h_{\rm f}=(\cos\theta)^2+4h_{\rm f}\sin\theta\,\cos\phi\,, \tag{38}$$

which always has $(\theta,\phi)=(\frac{\pi}{2},0)$ as its solution. For all $h_{\rm f}\geqslant\frac{1}{2}$, it is the only possible solution. However, for every $h_{\rm f}\in[0,\frac{1}{2})$, Eq. (38) has more than one solutions. A trajectory in Fig. 13 represents a subset of solutions for a given $h_{\rm f}$.

In this paragraph, we borrow some results from [9]. Since $(\theta_{\rm in},\phi_{\rm in})=(\frac{\pi}{2},0)$ is a fixed point of classical equations of motion (24), we take $\theta_{\rm in}=\frac{\pi}{2}-\epsilon$ to start the motion, where $\epsilon>0$ is a very small number. Up to the order of ϵ^2, we get the same energy conservation equation (38) for the new $\theta_{\rm in}$. Picking $\epsilon=10^{-3}$, we plot the

classical trajectories of $\mathbf{s}_{\rm cl}$ of (23) for different $h_{\rm f} \in (0, \frac{1}{2})$. Each trajectory represents a periodic motion of the unit vector $\mathbf{s}_{\rm cl}$. Corresponding to the (approximate) turning point $\mathbf{s}_{\rm cl} = (4h_{\rm f}-1, 0, \sqrt{1-(4h_{\rm f}-1)^2})$ displayed in blue or green color in Fig. 13, we have $\theta_{\rm tp} = \arcsin|4h_{\rm f}-1|$ and $\phi_{\rm tp} = 0$ or π. From $\theta_{\rm tp}$ to $\theta_{\rm in}$, the angle θ takes the half time period, hence we get

$$\begin{aligned}\frac{T_{\rm cl}}{2} &= 4\int_{\theta_{\rm tp}}^{\theta_{\rm in}} \frac{\sin\theta\, d\theta}{\cos\theta\sqrt{(\cos\theta_{\rm tp})^2-(\cos\theta)^2}} \\ &= -4\,\frac{1}{\cos\theta_{\rm tp}}\ln\left(\frac{\frac{\cos\theta_{\rm in}}{\cos\theta_{\rm tp}}}{1+\sqrt{1-\left(\frac{\cos\theta_{\rm in}}{\cos\theta_{\rm tp}}\right)^2}}\right) \\ &\approxeq -4\,\frac{1}{\cos\theta_{\rm tp}}\ln\left(\frac{\epsilon}{\cos\theta_{\rm tp}+\sqrt{(\cos\theta_{\rm tp})^2-\epsilon^2}}\right).\end{aligned} \tag{39}$$

The first equation in (39) is derived from the first equation in (24) with the help of (38). After the integration, we reach the second expression. Then, after applying $\cos\theta_{\rm in} = \sin\epsilon \approx \epsilon$, we arrive at the last expression in (39), which is slightly different than the one achieved in [9]. For all $0 \leqslant h_{\rm f} \leqslant \frac{1}{2}$, the time period $T_{\rm cl}$ diverges as $\epsilon \to 0$, and there are two kinds of divergences.

Logarithmic divergence: when $0 < h_{\rm f} < \frac{1}{2}$, then $\cos\theta_{\rm tp}$ is nonzero, and the divergence is due to $\ln(\epsilon)$ only, as reported in [9]. For example, let us take $4h_{\rm f} = 1$, then we get $\cos\theta_{\rm tp} = 1$ and $\frac{T_{\rm cl}}{2} \approxeq -4\ln(\frac{\epsilon}{2})$, which is similar to the results presented in (35) and (36).

Power-law divergence: when $h_{\rm f} \to 0$ or $\frac{1}{2}$, then we also have a divergence due to $\cos\theta_{\rm tp} \to 0$. To combine both the limits, we propose an association $\theta_{\rm tp} := \frac{\pi}{2} - 2\epsilon$. By the association, $\epsilon \to 0$ will automatically execute the limit $h_{\rm f} \to 0$ or $\frac{1}{2}$. Moreover, we get $\cos\theta_{\rm tp} = \sin(2\epsilon) \approx 2\epsilon$ and then

$$\frac{T_{\rm cl}}{2} \approx \frac{2\ln(2+\sqrt{3})}{\epsilon} = 2\ln(2+\sqrt{3})\, j^{\kappa}, \tag{40}$$

where $\kappa > 0$. The first and last expressions in (40) come from (39) and the relation $\epsilon := \frac{1}{j^{\kappa}}$ is proposed in the text around (35).

The above analysis suggests logarithmic and power-law divergences of $T_{\rm cl}$. To check this for different system sizes, we numerically computed the exact $\frac{T}{2}$, when the x-component of $\mathbf{s}$ of (23) reaches its first minimum value. For distinct $h_{\rm f}$, we present $\frac{T_j}{2}$ versus j plots in Fig. 14 with their best fit functions $\mathsf{g}(j)$, which are entered in Table III. The functions g are acquired by following the least squares method of Appendix E. In Appendix F, for $h_{\rm f} = 0$ and $j \geqslant 1$, we have analytically shown

$$\frac{T}{2} = \tau = \begin{cases} 4\pi j & \text{when } j \text{ is an integer} \\ 2\pi j & \text{when } j \text{ is a half-integer} \end{cases} \tag{41}$$

[see also the top-left plot in Fig. 14]. With the figure, table, and (41), one can deduce that the time period indeed follows a power-law divergence when $h_{\rm f}$ is 0 or $\frac{1}{2}$ and follows a logarithmic divergence when $h_{\rm f}$ is in the middle. If one puts $\epsilon := \frac{1}{\alpha\, j^{\kappa}}$ in (40), then she can find the values of α and κ for which $\frac{T_{\rm cl}}{2}$ become equal to $\mathsf{g}(j)$ given in Table I for $h_{\rm f} = 0.5$.

In the figure and table, we also present $\frac{T_j}{2}$ with its g for $h_{\rm f} = 0.6$, which reveals a convergent behavior of T_j against j. Such convergent behavior exists for all $h_{\rm f} > \frac{1}{2}$. For a higher $h_{\rm f}$, T_j converges faster and to a smaller value. Since there is a single point $(1,0,0)$ for the whole paramagnetic phase specified by $h_{\rm f} > \frac{1}{2}$, we cannot use the classical analysis to study the dynamics induced by a quench from $h_{\rm in} = \infty$ to $h_{\rm f} \in (\frac{1}{2}, \infty)$ for a finite N. The x-component of $\mathbf{s}$ goes to 1 as N grows for a quench within the paramagnetic phase.

Before moving to the next subsection, let us note that $|\psi_{\rm in}\rangle = |j\rangle_x$ and therefore $|\psi(t)\rangle$ are eigenkets of the spin-flip operator X due to its commutation with the Hamiltonian given in (2). As a result, we have

TABLE III. The best fit functions for the half time period. For $h_{\rm in} \to \infty$, the best fit functions $\mathsf{g}(j)$ for $\frac{T_j}{2}$ are recorded here with their MSE like Table I. In fact, $h_{\rm f} = 0.25$ corresponds to the same situation here as well as in Table I. The time period $T_{\rm cl}$ comes from (39) and (40) after taking the limit $\epsilon \to 0$.

$h_{\rm f}$	$T_{\rm cl}/2$	$\mathsf{g}(j)$	MSE
0.25	∞	$6.43944 + 2.01593\,\ln(j)$	0.00002146
0.5	∞	$3.68886\, j^{\,0.253}$	0.00001279
0.6		$6.51234 - 9.17933\, j^{-0.61}$	0.00002317

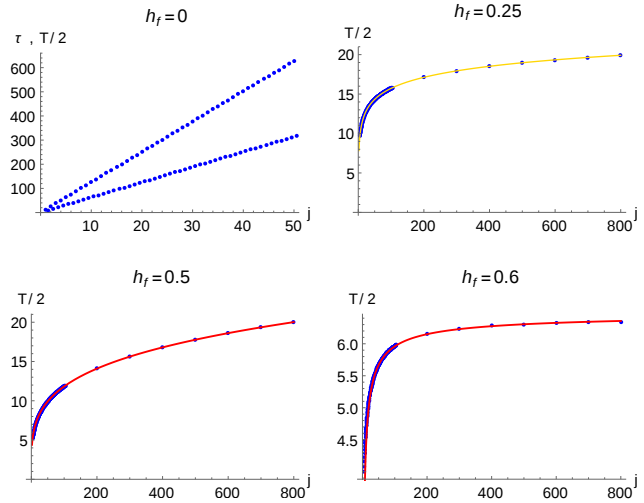

FIG. 14. The half time period versus system size. In each plot, the associated $h_{\rm f}$-value is placed at the top, and $\frac{T_j}{2}$ are depicted through the blue points for a sequence of j-values. The red (power-law) and yellow (logarithmic) curves portray the g functions listed in Table. III that best fit the (data) blue points. In the case of $h_{\rm f} = 0$, the two straight lines of points follow (41).

$\langle\psi(t)|J_z|\psi(t)\rangle = 0$ for all $t \geqslant 0$. So, rather than taking the z-component of $\mathbf{s}$ of (23), we have taken above its x-component as it is related to the dynamical order parameter $\mathsf{m}' := \lim_{\varsigma\to\infty}\int_0^\varsigma\langle(\frac{J_z}{j})^2\rangle\,dt$ considered in [9]. Recall that $\langle(J_z)^2\rangle$ and $\langle J_x\rangle$ are related through the energy conservation $\langle\psi_{\rm in}|H_{\rm f}|\psi_{\rm in}\rangle = -\frac{1}{4j}\langle(J_z)^2\rangle - h_{\rm f}\langle J_x\rangle$ for all $t \geqslant 0$ [see (38)]. If one of the expectation values increases with t, then the other will decrease except in the case of $h_{\rm f} = 0$ [see Appendix F].

Like (39), one can obtain

$$\begin{aligned}\mathsf{m}_{\rm cl} &:= \frac{2}{T_{\rm cl}}\int_{\frac{T_{\rm cl}}{2}}^{T_{\rm cl}}\cos\theta\,dt\\ &= \frac{8}{T_{\rm cl}}\int_{\theta_{\rm tp}}^{\theta_{\rm in}}\frac{\sin\theta\,d\theta}{\sqrt{(\cos\theta_{\rm tp})^2-(\cos\theta)^2}}\\ &= -\frac{8}{T_{\rm cl}}\cos\theta_{\rm tp}\left[\arcsin\left(\frac{\cos\theta_{\rm in}}{\cos\theta_{\rm tp}}\right)-\frac{\pi}{2}\right] \quad \text{and} \quad (42)\\ \mathsf{m}'_{\rm cl} &:= \frac{2}{T_{\rm cl}}\int_{\frac{T_{\rm cl}}{2}}^{T_{\rm cl}}(\cos\theta)^2\,dt\\ &= \frac{8}{T_{\rm cl}}\cos\theta_{\rm tp}\sqrt{1-\left(\frac{\cos\theta_{\rm in}}{\cos\theta_{\rm tp}}\right)^2}\end{aligned}$$

by taking $\theta_{\rm in} = \frac{\pi}{2} - \epsilon$, where $\epsilon > 0$. A slightly different expression of $\mathsf{m}'_{\rm cl}$ is achieved in [9], where it is shown that m' reaches its peak value at $4h_{\rm f} = 1$, and the value goes to zero as a multiple of $\frac{1}{\ln(j)}$ in the classical limit $j \to \infty$. Provided $h_{\rm f}$ does not approach to 0 or $\frac{1}{2}$ (that is, $\cos\theta_{\rm tp} \neq 0$), we have $\mathsf{m}_{\rm cl} \approx \frac{4\pi}{T_{\rm cl}}\cos\theta_{\rm tp}$ and $\mathsf{m}'_{\rm cl} \approx \frac{8}{T_{\rm cl}}\cos\theta_{\rm tp}$ for a sufficiently small ϵ. Particularly at $4h_{\rm f} = 1$, we have $\cos\theta_{\rm tp} = 1$, hence we get $\mathsf{m}_{\rm cl} \approx \frac{4\pi}{T_{\rm cl}}$ same as (32) and $\mathsf{m}'_{\rm cl} \approx \frac{8}{T_{\rm cl}}$. And, due to the logarithmic divergence of $T_{\rm cl}$ discussed above, m also goes to zero as a multiple of $\frac{1}{\ln(j)}$ in the classical limit.

In the case of $h_{\rm f} \to 0$ or $\frac{1}{2}$, we run an analysis similar to (40) for $\mathsf{m}_{\rm cl}$ as well as $\mathsf{m}'_{\rm cl}$ by taking $\theta_{\rm tr} = \frac{\pi}{2} - 2\epsilon$ and obtain

$$\begin{aligned}\mathsf{m}_{\rm cl} &\approx \frac{4\pi}{3\ln(2+\sqrt{3})}\,\epsilon^2 = \frac{4\pi}{3\ln(2+\sqrt{3})}\,j^{-2\kappa} \quad \text{and}\\ \mathsf{m}'_{\rm cl} &\approx \frac{2\sqrt{3}}{\ln(2+\sqrt{3})}\,\epsilon^2 = \frac{2\sqrt{3}}{\ln(2+\sqrt{3})}\,j^{-2\kappa} \qquad (43)\end{aligned}$$

from (42). Result (43) suggests a *power-law decay* of m and m' with the system size when $h_{\rm f}$ is very near to 0 or $\frac{1}{2}$.

Strictly speaking, we have the energy gap $\Delta \neq 0$ when $0 < h_{\rm in}, j < \infty$ as discussed in Sec. II, and $\langle J_z\rangle = 0 = \mathsf{m}$ as $|\psi_{\rm in}\rangle = |e_0\rangle$ is an eigenket of X. However, for a finite j, when the gap becomes almost zero in the ferromagnetic phase ($\theta_0 < \frac{\pi}{2}$), the ground state-vector can be taken as one of the mean field kets, that is, $|\psi_{\rm in}\rangle = |\theta_0\rangle$ as per (7). Then, we get $\langle J_z\rangle \neq 0 \neq \mathsf{m}$ and the above results of m can be realized for a finite j and $2h_{\rm in} < 1$.

For $h_{\rm in} \to \infty$ and $h_{\rm f} = 0$, the exact $\mathsf{m} = 0$ and $\mathsf{m}' = \frac{1}{2j}$ for all j [see (F5)]. The dynamical order parameters $\mathsf{m}_{\rm cl}$ of (42) and m' are plotted in Fig. 16 and Ref. [9], respectively.

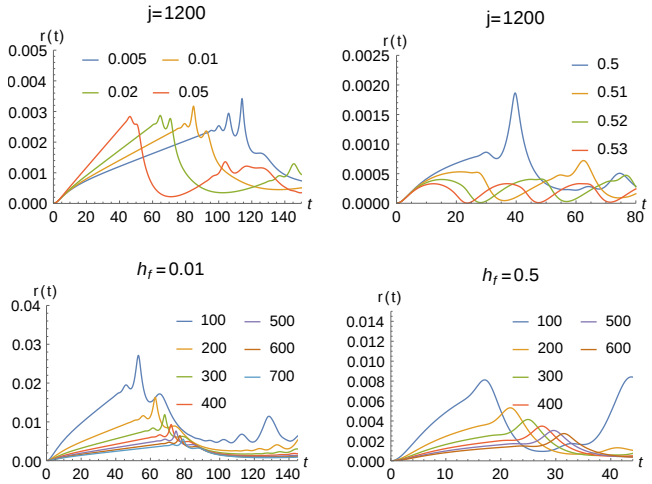

FIG. 15. The rate versus time. All the plots are for $h_{\rm in} \to \infty$. In the first row, for the system size 2×1200, the Loschmidt rate is exhibited in different colors for $h_{\rm f} = 0.005, \cdots, 0.53$ like Fig. 9. In the bottom row, for a fixed $h_{\rm f}$, the rate is displayed for $j = 100, \cdots, 700$ in separate colors like in Figs. 11 and 12. In Fig. 21, $1/p$ versus t plots reveal how does (not) kink develop with j in the case of $h_{\rm f} = \frac{1}{2}$ ($h_{\rm f} > \frac{1}{2}$).

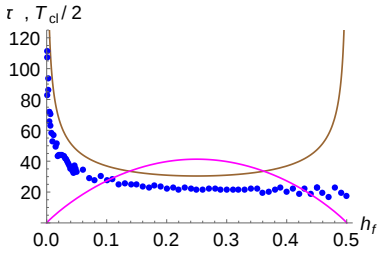

FIG. 16. First critical time versus final field strength. Having $j = 100$ and $|\psi_{\rm in}\rangle = |j\rangle_x$, here we present the first critical time τ for $h_{\rm f} = 0.0005, \cdots, 0.5$, which suggests $\tau \to \infty$ as $h_{\rm f} \to 0$ even for a finite system size. The brown curve represent—the last expression of (39) for $\epsilon = 10^{-3}$—the half time period as a function the field strength $h_{\rm f}$ like Fig. 10. All the blue points and the whole brown curve will go to infinity in the limits $j \to \infty$ [see Fig. 17] and $\epsilon \to 0$, respectively. The magenta curve portrays $100 \times \mathsf{m}_{\rm cl}$, where $\epsilon = 10^{-3}$ and the dynamical order parameter $\mathsf{m}_{\rm cl}$ is given in (42). In the limit $\epsilon \to 0$, we have $\mathsf{m}_{\rm cl} \to 0$ for every $h_{\rm f}$.

2. *DPT-II*

Figures 16, 17, and 22 as well as Tables IV and V in Appendix F hold our main results for this subsection. They basically present how the critical time τ and the rate $r(\tau)$ perform with growing number $N = 2j$ of spins. Here τ diverges logarithmically or with a power-law like T

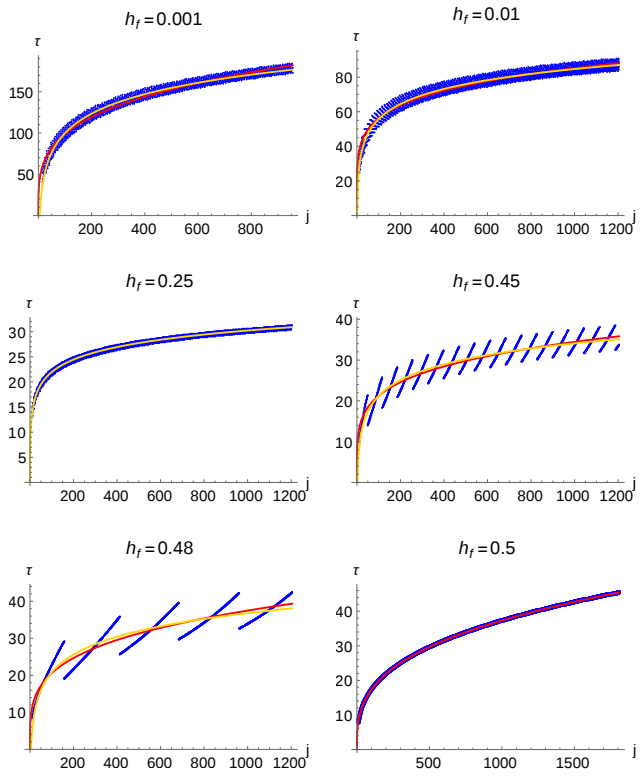

FIG. 17. First critical time versus system size. Similar to Figs. 11 and 12, all these plots are for $h_{\rm in} \to \infty$, that is, $|\psi_{\rm in}\rangle = |j\rangle_x$. The blue points represent the exact data $\{\tau_j\}$ procured for the $h_{\rm f}$-values stated at the top of each plot. Like Sec. III A 2, here the data show oscillations of τ with respect to j except in the case of $h_{\rm f} = 0.5$. The red and yellow curves exhibit the power-law and logarithmic best fit functions g, respectively, from Table IV. As we go from $h_{\rm f} = 0.001$ to $h_{\rm f} = 0.5$, the color of curves is changing from red to yellow to red, which reflects the change of functional form of g in Table IV. The plots for $h_{\rm f} = 0.001, 0.01, 0.45, 0.48$ carry both the red and yellow curves.

in the previous subsection, and $r(\tau)$ goes to zero provided $h_{\rm f}$ is nonzero.

Now let us recall the rate $r(t)$ from (26) to study the DPT-II in the case where all the spins are initially polarized in the x-direction, $|\psi_{\rm in}\rangle = |j\rangle_x$. Keeping the system size fixed, we plot $r(t)$ for different $h_{\rm f}$ in the top row in Fig. 15. There one can observe that the first cusp appears at the first peak of $r(t)$ when $h_{\rm f} \in [0, \frac{1}{2}]$ and no cusp appears when $\frac{1}{2} < h_{\rm f}$. This identifies the regular ($h_{\rm f} \leqslant \frac{1}{2}$) and trivial ($\frac{1}{2} < h_{\rm f}$) phases [69, 70]. As we increase the final field's strength from 0 to $\frac{1}{2}$, the first kink shifts towards the left-hand side, which implies that the first critical time τ decreases with $h_{\rm f}$. This is presented in Fig. 16, where one can notice that both τ and the time period of (39) follow similar behavior with $h_{\rm f}$ except around $\frac{1}{2}$.

Now we demonstrate, for a fixed $h_{\rm f}$, how τ behaves with increasing system size $N = 2j$. Plots in the second row in Fig. 15 reveal that **(i)** the first kink moves towards the right-hand side, which indicates that τ_j grows with j towards infinity. **(ii)** The height of the kink (or peak) decreases towards zero as j goes to infinity provided $h_{\rm f} \neq 0$. Observations **(i)** and **(ii)** are justified by the exact data $\{\tau_j\}$ and $\{Nr(\tau_j)\}$ plotted in Figs. 17 and 22, respectively. Table V provides the best fit functions for the data $\{Nr(\tau_j)\}$, which suggests a power-law decay of $r(\tau_j)$ to zero as j goes to infinity.

Now let us focus on observation **(i)**. The best fit function $\mathsf{g}(j)$ for the data $\{\tau_j\}$ are displayed in Fig. 17 and listed in Table IV with their $h_{\rm f}$-values. There one can see that, when $h_{\rm f} = 0.001$ is close to 0 or $h_{\rm f} = \frac{1}{2}$, $\mathsf{g}(j)$ represents a *power-law divergence* of the critical time with the system size. Whereas, $\mathsf{g}(j)$ suggests a *logarithmic divergence* when $h_{\rm f} = \frac{1}{4}$ is in-between zero and one half. The same behavior is exhibited by the time period T in Sec. III B 1.

TABLE IV. The best fit functions for the first critical time. For $h_{\rm in} \to \infty$, the best fit functions g for τ are recorded here with their MSE like Table II. The data $\{\tau_j\}$ with their $\mathsf{g}(j)$ are plotted in Fig. 17. Here as we go from top to bottom the functional form (divergent nature) of g changes from power-law to logarithmic to power-law. We have witnessed the same behavior in Table III in the case of T. For $h_{\rm f} = 0$, τ is stated in (41) and exhibited in the top-left plot of Fig. 14. Two different functions have almost the same mean square errors in the case of $h_{\rm f} \in \{0.01, 0.45, 0.48\}$, so we place both of them in the table. Since τ-values are bigger when $h_{\rm f} = 0.001$ [see Figs. 16 and 17], MSE has the highest value in the table. Whereas, in the case of $h_{\rm f} = 0.48$, the higher MSE is due to the large oscillations in the data $\{\tau_j\}$ [see Fig. 17].

$h_{\rm f}$	$\mathsf{g}(j)$	MSE
0.001	$28.5477\, j^{\,0.27}$	26.9484
	$-57.049 + 34.0667\, \ln(j)$	22.1394
0.01	$24.5648\, j^{\,0.18}$	7.5734
	$-2.08403 + 12.5588\, \ln(j)$	6.20107
0.25	$5.43838 + 3.59017\, \ln(j)$	0.131998
0.45	$-4.55339 + 5.59268\, \ln(j)$	4.03251
	$8.07602\, j^{\,0.21}$	4.0818
0.48	$-11.2193 + 6.95091\, \ln(j)$	7.99994
	$6.22128\, j^{\,0.26}$	7.68492
0.5	$3.7667\, j^{\,0.332}$	0.0005797

IV. SUMMARY

The first and second parts of the paper separately deal with the equilibrium and dynamical properties of the spin system in the FCIM. In the first part, for a finite system, we have demonstrated that the approximate $|\chi\rangle$ and the associated exact energy eigenkets $|e\rangle$ show a large overlap provided we do not go too close to the equilibrium phase transition point. In addition, we have captured the

energy gap and entanglement properties of the ground and first excited states through $|\chi\rangle$. We have found a good agreement between approximate and exact results in the case of energy gap and geometric entanglement (an N-body entanglement quantifier). Whereas, the concurrence (a two-body entanglement measure) shows a good match only in the paramagnetic phase.

In the second part, we have exhibited that the time period T in the DPT-I and the first critical time τ in the DPT-II exhibit similar converging or diverging behaviors with respect to the system size. Initially if all the spins are in the z-direction with respect to Hamiltonian (1), both T and τ diverge *logarithmically* with the number N of spins at the dynamical phase transition point $h_{\rm f} = \frac{1}{4}$. If all the spins are in the x-direction at the beginning, then both T and τ diverge over the whole interval $[0, \frac{1}{2}]$ where $h_{\rm f}$ lies. At the endpoints of the interval, the divergence is through a *power-law*, and it is logarithmic in the middle. It will be interesting to run a similar investigation for the DPTs in other mean-field models studied in [43–45, 47, 49, 50].

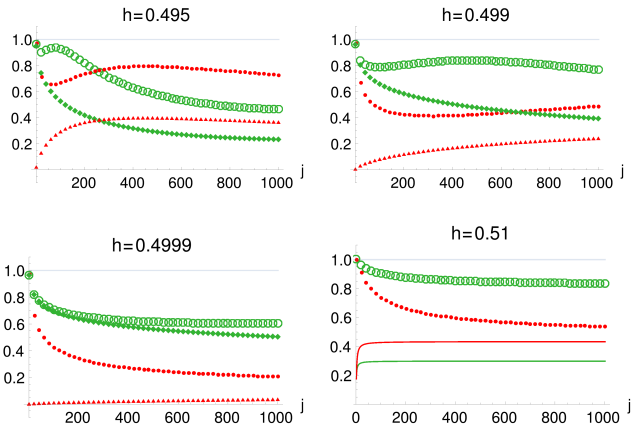

FIG. 18. Overlap versus system size. It is an extension of Fig. 1. Here the h-values are taken near the equilibrium phase transition point $h = 0.5$.

ACKNOWLEDGMENTS

We acknowledge support through the "QuEST" program of the Department of Science and Technology, Government of India. For the numerical computations, we are grateful to the cluster computing facility at the Harish-Chandra Research Institute, India.

Appendix A: Easy way to check (9) in the $\mathcal{B}_x$ basis

The Dicke kets of (3) and the spin coherent kets of (6) can be explicitly written as [81, 83]

$$|m\rangle_z = \frac{1}{\sqrt{\binom{2j}{j+m}}}\left(|\uparrow_z\rangle^{\otimes j+m}|\downarrow_z\rangle^{\otimes j-m} + \text{per}\right) \quad \text{and}$$
$$|\theta,\phi\rangle = \left(\cos\tfrac{\theta}{2}|\uparrow_z\rangle + \sin\tfrac{\theta}{2}\,e^{{\rm i}\phi}|\downarrow_z\rangle\right)^{\otimes 2j}\,, \tag{A1}$$

respectively, where $|\uparrow_z,\downarrow_z\rangle$ are the $+1,-1$ eigenvalue kets of the single-spin Pauli operator σ^z, and 'per' denotes all possible permutations. Then, the mean-field coherent kets characterized by (7) can be expressed as

$$\begin{aligned}
|\theta_0\rangle &= \left(\sqrt{\tfrac{1+\sqrt{1-(2h)^2}}{2}}|\uparrow_z\rangle + \sqrt{\tfrac{1-\sqrt{1-(2h)^2}}{2}}|\downarrow_z\rangle\right)^{\otimes 2j} \\
&= \left(\sqrt{\tfrac{1+2h}{2}}|\uparrow_x\rangle + \sqrt{\tfrac{1-2h}{2}}|\downarrow_x\rangle\right)^{\otimes 2j} \\
&= \sum_{m=-j}^{j}\binom{2j}{j+m}^{\frac{1}{2}}\left(\tfrac{1+2h}{2}\right)^{\frac{j+m}{2}}\left(\tfrac{1-2h}{2}\right)^{\frac{j-m}{2}}|m\rangle_x\,, \\
|\pi-\theta_0\rangle &= \sum_{m=-j}^{j}\binom{2j}{j+m}^{\frac{1}{2}}\left(\tfrac{1+2h}{2}\right)^{\frac{j+m}{2}}\left(\tfrac{1-2h}{2}\right)^{\frac{j-m}{2}}\times \\
&\qquad (-1)^{j-m}\,|m\rangle_x\,,
\end{aligned} \tag{A2}$$

where $|\uparrow_x,\downarrow_x\rangle = \frac{1}{\sqrt{2}}(|\uparrow_z\rangle \pm |\downarrow_z\rangle)$ denotes single spin-up and spin-down, respectively, in the x-direction.

Now we can represent the χ-kets of (8) in the eigenbasis $\mathcal{B}_x := \{|m\rangle_x\}$ of J_x as

$$\begin{aligned}
|\chi_+\rangle &= \sqrt{\tfrac{2}{1+(2h)^{2j}}}\sum_{k=0}^{\lceil j-\frac{1}{2}\rceil}\binom{2j}{2k}^{\frac{1}{2}}\left(\tfrac{1+2h}{2}\right)^{j-k}\times \\
&\qquad \left(\tfrac{1-2h}{2}\right)^{k}|j-2k\rangle_x \qquad \text{and} \\
|\chi_-\rangle &= \sqrt{\tfrac{2}{1-(2h)^{2j}}}\sum_{k=0}^{\lfloor j-\frac{1}{2}\rfloor}\binom{2j}{2k+1}^{\frac{1}{2}}\left(\tfrac{1+2h}{2}\right)^{j-k-\frac{1}{2}}\times \\
&\qquad \left(\tfrac{1-2h}{2}\right)^{k+\frac{1}{2}}|j-(2k+1)\rangle_x\,,
\end{aligned} \tag{A3}$$

where $\lceil\ \rceil$ and $\lfloor\ \rfloor$ are the ceiling and floor functions. By a direct inspection one can check that the actual eigenkets

are of the form

$$|e_0\rangle = \sum_{k=0}^{\lceil j-\frac{1}{2}\rceil} |j-2k\rangle_x\langle j-2k|e_0\rangle \in \mathcal{E}_+ \quad \text{and} \tag{A4}$$
$$|e_1\rangle = \sum_{k=0}^{\lfloor j-\frac{1}{2}\rfloor} |j-(2k+1)\rangle_x\langle j-(2k+1)|e_1\rangle \in \mathcal{E}_-$$

for all $0 < h, j < \infty$ (see also Eq. (4) in [32]), and then one can justify (9) using (A2)–(A4).

Appendix B: Energy minimization in the paramagnetic phase

Here the task is to find $|\chi\rangle$ [see (12)]—in the two-dimensional space spanned by $\mathsf{B}_x := \{|m\rangle_x, |m'\rangle_x\}$, where $j-3 \leqslant m' = m-2$—that provides the minimum energy $\varepsilon := \langle\chi|H|\chi\rangle$. To complete the task, we restrict Hamiltonian (4) onto span(B_x), then the restricted Hamiltonian in the basis B_x is represented by

$$H\Big|_{\mathsf{B}_x} \equiv \begin{pmatrix} {}_x\langle m|H|m\rangle_x & {}_x\langle m|H|m'\rangle_x \\ {}_x\langle m'|H|m\rangle_x & {}_x\langle m'|H|m'\rangle_x \end{pmatrix} =: -\underbrace{\begin{pmatrix} a & b \\ b & c \end{pmatrix}}_{M} \tag{B1}$$

where $a, c \in \mathbb{R}$ and $b \geqslant 0$ for all $j \geqslant 1$. The eigenvalues and eigenvectors of M are

$$\begin{aligned} \zeta_\pm &= \frac{(a+c) \pm \text{Disc}}{2} \quad \text{and} \\ |\zeta_\pm\rangle &= \sqrt{\tfrac{1\pm\cos\mu}{2}}\,|m\rangle_x \pm \sqrt{\tfrac{1\mp\cos\mu}{2}}\,|m'\rangle_x\,, \text{ where} \\ \cos\mu &= \frac{a-c}{\text{Disc}}\,, \quad \sin\mu = \frac{2b}{\text{Disc}}\,, \quad \text{and} \\ \text{Disc} &= \sqrt{(a-c)^2+(2b)^2}\,. \end{aligned} \tag{B2}$$

Clearly $|\chi\rangle = |\zeta_+\rangle \in \text{span}(\mathsf{B}_x)$ will provide the minimum energy $\varepsilon = -\zeta_+ < 0$, and $\mu \in [0, \pi]$. If one wants even better approximation of the ground and first excited states then she can repeat the above method by taking a larger set, say, $\mathsf{B}_x = \{|m\rangle_x, |m'\rangle_x, |m''\rangle_x\}$ where $m''+4 = m'+2 = m = j$ or $j-1$.

In the case of $|\chi_0\rangle$ [see (12)], we have $m = j$ and get

$$\begin{aligned} \mu_0 &= \arccos\left(\frac{4h-1+\frac{1}{j}}{2\,\text{Disc}}\right), \\ \varepsilon_0 &= -\tfrac{1}{2}\left(\tfrac{6j-4}{8j} + 2h(j-1) + \text{Disc}\right), \quad \text{and} \\ \text{Disc} &= \tfrac{1}{2}\sqrt{\left(4h-1+\tfrac{1}{j}\right)^2 + \tfrac{j(2j-1)}{(2j)^2}}\,. \end{aligned} \tag{B3}$$

In the case of $|\chi_1\rangle$, $m = j-1$, and we obtain

$$\begin{aligned} \mu_1 &= \arccos\left(\frac{4h-1+\frac{2}{j}}{2\,\text{Disc}}\right), \\ \varepsilon_1 &= -\tfrac{1}{2}\left(\tfrac{10j-10}{8j} + 2h(j-2) + \text{Disc}\right), \quad \text{and} \\ \text{Disc} &= \tfrac{1}{2}\sqrt{\left(4h-1+\tfrac{2}{j}\right)^2 + \tfrac{3(j-1)(2j-1)}{(2j)^2}}\,. \end{aligned} \tag{B4}$$

In the classical limit, we get the approximate energy gap

$$\begin{aligned} \lim_{j\to\infty}(\varepsilon_1 - \varepsilon_0) &= h - \tfrac{1}{4} + \tfrac{1}{4}\left(\sqrt{(4h-1)^2+\tfrac{1}{2}} - \sqrt{(4h-1)^2+\tfrac{3}{2}}\right) \\ &\approx h - \tfrac{1}{4} \quad \text{for a large } h\,. \end{aligned} \tag{B5}$$

Appendix C: Concurrence of $|\chi\rangle\langle\chi|$

We have N-body symmetric quantum states such as $|\chi\rangle\langle\chi|$ and $|e\rangle\langle e|$ in Sec. II, and here we are interested in their quantum entanglement. It is shown in [86] that, for every symmetric state, the two-body reduced density matrix can be expressed as

$$\rho = \begin{pmatrix} a_+ & d_+^* & d_+^* & b^* \\ d_+ & c & c & d_-^* \\ d_+ & c & c & d_-^* \\ b & d_- & d_- & a_- \end{pmatrix}, \quad \text{where} \tag{C1}$$
$$\begin{aligned} a_\pm &= \tfrac{1}{4}\left(1 \pm \tfrac{4\langle J_z\rangle}{N} + \tfrac{4\langle J_z^2\rangle - N}{N^2-N}\right), \\ b &= \tfrac{\langle J_x^2\rangle - \langle J_y^2\rangle + \mathrm{i}\langle [J_x, J_y]_+\rangle}{N^2-N}\,, \\ c &= \tfrac{N^2 - 4\langle J_z^2\rangle}{4(N^2-N)}\,, \\ d_\pm &= \tfrac{1}{2}\left(\tfrac{\langle J_x\rangle + \mathrm{i}\langle J_y\rangle}{N} \pm \tfrac{\langle [J_x, J_z]_+\rangle + \mathrm{i}\langle [J_y, J_z]_+\rangle}{N^2-N}\right), \end{aligned}$$

and $[A, B]_+ := AB + BA$. The matrix in (C1) is in the basis $\{|\uparrow_z\uparrow_z\rangle, |\uparrow_z\downarrow_z\rangle, |\downarrow_z\uparrow_z\rangle, |\downarrow_z\downarrow_z\rangle\}$, and all the expectation values are computed with the parent N-spin state from which ρ is obtained.

Since both $|\chi\rangle$ and $|e\rangle$ are eigenkets of the spin-flip operator X [given in (2)] for $0 < h, j < \infty$, and X anticommutes with J_y, J_z, J_xJ_y, and J_xJ_z, we get the zero expectation values

$$\langle J_y\rangle = \langle J_z\rangle = \langle [J_x, J_y]_+\rangle = \langle [J_x, J_z]_+\rangle = 0 \tag{C2}$$

from both the keys. Furthermore, as all the coefficients ${}_z\langle m|\chi\rangle$ and ${}_z\langle m|e\rangle$ of the two kets are real numbers in the basis $\mathcal{B}_z$ of (3), the matrix in (C1) will be real (that is, $\rho = \rho^*$), and thus $\langle [J_y, J_z]_+\rangle = 0$. So, in the case of approximate $|\chi\rangle$ and exact $|e\rangle$ eigenkets of Hamiltonian

(4), (C1) turns into

$$\rho = \begin{pmatrix} a & d & d & b \\ d & c & c & d \\ d & c & c & d \\ b & d & d & a \end{pmatrix}, \quad \text{where}$$
$$a = \frac{1}{4}\left(1 + \frac{4\langle J_z^2\rangle - N}{N^2 - N}\right),\ b = \frac{\langle J_x^2\rangle - \langle J_y^2\rangle}{N^2 - N}, \qquad \text{(C3)}$$
$$c = \frac{N^2 - 4\langle J_z^2\rangle}{4(N^2 - N)},\ d = \frac{\langle J_x\rangle}{2N},$$

and we get the eigenvalues

$$\begin{aligned} \lambda_1 &= 0 \\ \lambda_2 &= (a-b)^2 \qquad \text{(C4)} \\ \lambda_3 &= \tfrac{(a+b)^2+4(c^2-2d^2)+(a+b-2c)\sqrt{(a+b+2c)^2-16d^2}}{2} \\ \lambda_4 &= \tfrac{(a+b)^2+4(c^2-2d^2)-(a+b-2c)\sqrt{(a+b+2c)^2-16d^2}}{2} \end{aligned}$$

of $\rho\,\widetilde{\rho}$ for concurrence (15). In the case of exact ground and first excited energy eigenkets $|e_{0,1}\rangle$, we exploit (C3) and (C4) to numerically compute the concurrence and present the results in Fig. 4.

In the case of $|\chi_\pm\rangle\langle\chi_\pm|$, $\theta = \theta_0$, we get

$$\begin{aligned} a^{(\pm)} &= \frac{1 + \cos\theta^2 \pm \sin\theta^N}{4\,(1 \pm \sin\theta^N)}, \\ b^{(\pm)} &= \frac{\sin\theta^2 \pm (1+\cos\theta^2)\sin\theta_0^{N-2}}{4\,(1 \pm \sin\theta^N)}, \\ c^{(\pm)} &= \frac{\sin\theta^2(1 \pm \sin\theta^{N-2})}{4\,(1 \pm \sin\theta^N)}, \quad \text{and} \\ d^{(\pm)} &= \frac{\sin\theta(1 \pm \sin\theta^{N-2})}{4\,(1 \pm \sin\theta^N)}, \end{aligned} \qquad \text{(C5)}$$

which give

$$\begin{aligned} \lambda_2 &= \frac{\cos\theta^4(1 \mp \sin\theta^{N-2})^2}{4\,(1 \pm \sin\theta^N)^2}, \\ \lambda_3 &= \frac{\cos\theta^4(1 \pm \sin\theta^{N-2})^2}{4\,(1 \pm \sin\theta^N)^2}, \quad \text{and} \\ \lambda_4 &= 0, \quad \text{and thus} \\ \mathsf{C}_{\chi_\pm} &= \pm\sqrt{\lambda_3} \mp \sqrt{\lambda_2}. \end{aligned} \qquad \text{(C6)}$$

The concurrences $\mathsf{C}_{\chi_\pm}$ of $|\chi_\pm\rangle$ is rewritten in (16) and plotted in Fig. 4.

Since the kets $|\chi_{0,1}\rangle$ in (12) are expressed in the basis $\mathcal{B}_x = \{|m\rangle_x\}_{m=-j}^{j}$, it is easy to represent their reduced density matrix

$$\rho_x = \begin{pmatrix} v & 0 & 0 & u \\ 0 & w & w & 0 \\ 0 & w & w & 0 \\ u & 0 & 0 & v' \end{pmatrix} \qquad \text{(C7)}$$

in the basis $\{|\uparrow_x\uparrow_x\rangle, |\uparrow_x\downarrow_x\rangle, |\downarrow_x\uparrow_x\rangle, |\downarrow_x\downarrow_x\rangle\}$. The matrices in (C3) and (C7) are related via the local unitary transformation $\rho = \mathsf{H}\otimes\mathsf{H}(\rho_x)\mathsf{H}\otimes\mathsf{H}$, where the Hadamard operator H interchanges the bases as $|\uparrow_x\rangle \leftrightarrow |\uparrow_z\rangle$ and $|\downarrow_x\rangle \leftrightarrow |\downarrow_z\rangle$. Since $\mathsf{H}\otimes\mathsf{H}$ commutes with $\sigma_y\otimes\sigma_y$, we get $\rho\widetilde{\rho} = \mathsf{H}\otimes\mathsf{H}(\rho_x\widetilde{\rho_x})\mathsf{H}\otimes\mathsf{H}$, and the eigenvalues of $\rho_x\widetilde{\rho_x}$ are

$$\begin{aligned} \lambda_1 &= 0\,, \quad \lambda_2 = (2w)^2\,, \\ \lambda_3 &= (\sqrt{v\,v'} + u\,)^2\,, \quad \text{and} \\ \lambda_4 &= (\sqrt{v\,v'} - u\,)^2\,. \end{aligned} \qquad \text{(C8)}$$

In the case of $|\chi_0\rangle$, we get

$$\begin{aligned} v &= (\cos\tfrac{\mu_0}{2})^2 + (\sin\tfrac{\mu_0}{2})^2\,\tfrac{(N-2)(N-3)}{N(N-1)} \approx 1\,, \\ v' &= (\sin\tfrac{\mu_0}{2})^2\,\tfrac{2}{N(N-1)} \approx (\sin\tfrac{\mu_0}{2})^2\,\tfrac{2}{N^2}\,, \\ u &= \sin\tfrac{\mu_0}{2}\cos\tfrac{\mu_0}{2}\sqrt{\tfrac{2}{N(N-1)}} \approx \sin\tfrac{\mu_0}{2}\cos\tfrac{\mu_0}{2}\,\tfrac{\sqrt{2}}{N}\,, \\ w &= (\sin\tfrac{\mu_0}{2})^2\,\tfrac{2(N-2)}{N(N-1)} \approx (\sin\tfrac{\mu_0}{2})^2\,\tfrac{2}{N}\,, \end{aligned} \qquad \text{(C9)}$$

where the approximation is taken under the condition $N \gg 1$. For $j \geqslant 1$, with (B3), (C8), and (C9), one can realize that the concurrence of $|\chi_0\rangle$ is [86]

$$\begin{aligned} \mathsf{C}_{\chi_0} &= 2\max\{(u-w), 0, (w - \sqrt{v\,v'}\,)\} \quad \text{for} \quad h \geqslant 0 \\ &= 2(u-w) \quad \text{for} \quad h \geqslant 0.5\,. \end{aligned} \qquad \text{(C10)}$$

In the case of $|\chi_1\rangle$, we attain

$$\begin{aligned} v &= (\cos\tfrac{\mu_1}{2})^2\,\tfrac{(N-2)}{N} + (\sin\tfrac{\mu_1}{2})^2\,\tfrac{(N-3)(N-4)}{N(N-1)} \approx 1\,, \\ v' &= (\sin\tfrac{\mu_1}{2})^2\,\tfrac{6}{N(N-1)} \approx (\sin\tfrac{\mu_1}{2})^2\,\tfrac{6}{N^2}\,, \\ u &= \sin\tfrac{\mu_1}{2}\cos\tfrac{\mu_1}{2}\,\tfrac{1}{N}\sqrt{\tfrac{6(N-2)}{N-1}} \approx \sin\tfrac{\mu_1}{2}\cos\tfrac{\mu_1}{2}\,\tfrac{\sqrt{6}}{N}\,, \\ w &= (\cos\tfrac{\mu_1}{2})^2\,\tfrac{1}{N} + (\sin\tfrac{\mu_1}{2})^2\,\tfrac{3(N-3)}{N(N-1)} \approx \tfrac{2-\cos\mu_1}{N}\,. \end{aligned} \qquad \text{(C11)}$$

For $j \geqslant 1$, with (B4), (C8), and (C11), we discover that the concurrence of $|\chi_1\rangle$ is

$$\mathsf{C}_{\chi_1} = 2\,(w - \sqrt{v\,v'}\,) \quad \text{for} \quad h \geqslant 0\,. \qquad \text{(C12)}$$

Concurrences (C10) and (C12) are restated in (16) and plotted in Fig. 4.

Appendix D: Geometric entanglement of $|\chi\rangle\langle\chi|$

The inner products between the coherent ket $|\vartheta, \phi = 0\rangle \equiv |\vartheta\rangle$ of (6) and the approximate eigenkets $|\chi\rangle$ of (8) and (12) are

$$\langle\vartheta|\chi_\pm\rangle = \frac{\cos(\frac{\vartheta-\theta_0}{2})^N \pm \sin(\frac{\vartheta+\theta_0}{2})^N}{\sqrt{2(1 \pm (\sin\theta_0)^N)}}\,, \qquad \text{(D1)}$$

$$\begin{aligned} \langle\vartheta|\chi_0\rangle &= \cos\tfrac{\mu_0}{2}\cos(\tfrac{\pi}{4} - \tfrac{\vartheta}{2})^N + \\ &\quad \sin\tfrac{\mu_0}{2}\,\sqrt{\tbinom{N}{2}}\cos(\tfrac{\pi}{4} - \tfrac{\vartheta}{2})^{N-2}\sin(\tfrac{\pi}{4} - \tfrac{\vartheta}{2})^2\,, \quad \text{and} \\ \langle\vartheta|\chi_1\rangle &= \cos\tfrac{\mu_1}{2}\,\sqrt{\tbinom{N}{1}}\cos(\tfrac{\pi}{4} - \tfrac{\vartheta}{2})^{N-1}\sin(\tfrac{\pi}{4} - \tfrac{\vartheta}{2}) + \\ &\quad \sin\tfrac{\mu_1}{2}\,\sqrt{\tbinom{N}{3}}\,\cos(\tfrac{\pi}{4} - \tfrac{\vartheta}{2})^{N-3}\sin(\tfrac{\pi}{4} - \tfrac{\vartheta}{2})^3\,. \end{aligned}$$

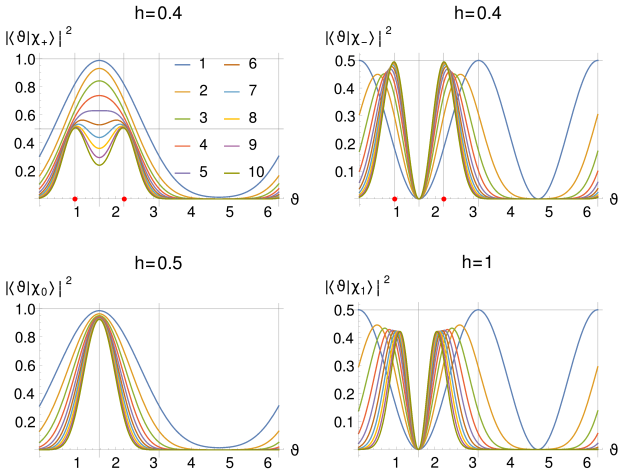

FIG. 19. Overlap between the coherent ket and approximate energy eigenkets. The absolute square of the inner products between the coherent ket $|\vartheta\rangle$ and the approximate eigenkets $|\chi\rangle$ is highlighted in distinct colors for $j = 1, \cdots, 10$. In all the pictures, the color-coding is the same. Graphs at the top belong to the ferromagnetic phase, $0 \leqslant 2h < 1$, where the red points indicate $\theta_0 = \arcsin(2h)$ and $\pi - \theta_0$ that are associated with $|\chi_\pm\rangle$. Graphs at the bottom are connected to $|\chi_{0,1}\rangle$ that are given for $1 \leqslant 2h$.

We plot their absolute squares as functions of ϑ in Fig. 19 for different $j = \frac{N}{2}$ and h. Recall the θ_0, μ_0, and μ_1 are functions of j and h as per (7), (B3), and (B4), respectively.

Appendix E: The least squares method

In Sec. III, we have studied the time period T and the first critical time τ as functions of j. They are obtained numerically by the exact diagonalization of Hamiltonian (4). As a result, we get a list of values f_j for a set of j. Here f represents T or τ. To find a function $\mathsf{g}(j)$ that best fits the data $\{f_j\}$, we adopt the least squares method described as follows.

We consider three kinds of functions

$$\begin{aligned} &\upsilon(c,j) \in \{j^c, \mathrm{e}^{c\,j}, \ln(j)\}\,, \quad \text{where} \\ &g(j) = a + b\;\upsilon(c,j) \quad \text{and} \\ &\mathrm{MSE} = \frac{1}{\Omega}\sum_j \left(f_j - g(j)\right)^2 \end{aligned} \tag{E1}$$

is the mean square error. Ω denotes the cardinality of the set $\{f_j\}$. By minimizing MSE over the real parameters $\{a, b, c\}$ and the three υ, we obtain the values $\{\mathsf{a}, \mathsf{b}, \mathsf{c}\}$ and the function $\boldsymbol{\upsilon}(\mathsf{c}, j)$ that provide the best fit $\mathsf{g}(j) = \mathsf{a} + \mathsf{b}\,\boldsymbol{\upsilon}(\mathsf{c}, j)$ for a given data-set, and the least error is $\mathsf{MSE} := \min_{a,b,c,\upsilon} \mathrm{MSE}$.

Diverging case: If the sequence f_j appears diverging to ∞, we fix $a = 0$ for $a + bj^c$ and $a + b\,\mathrm{e}^{c\,j}$, and then follow the above procedure. Moreover, we cannot pick $c < 0$ in (E1). In this case, through the best fit function, we report the nature of divergence: power-law j^{c}, exponential $\mathrm{e}^{\mathsf{c}\,j}$ or logarithmic $\mathsf{a} + \mathsf{b}\ln(j)$ (for example, see Tables III and IV).

Converging case: As j grows, if the sequence f_j seems converging to a known value $f_\infty := \lim_{j\to\infty} f_j$ then we take $a = f_\infty$ (for instance, see Table I), otherwise the obtained a will be our estimate for f_∞ (for example, see Table II). Here we cannot take υ to be $\ln(j)$ or $c > 0$ in (E1). If the best fit function turns out $\mathsf{g}(j) = \mathsf{a} + \mathsf{b}\,j^{\mathsf{c}}$ then $\mathsf{c} \leqslant 0$ will give an estimate of the log-log finite-size scaling because $\ln|\mathsf{g}(j) - \mathsf{a}| = \ln|\mathsf{b}| + \mathsf{c}\ln(j)$. If the best fit function comes out $\mathsf{g}(j) = \mathsf{a} + \mathsf{b}\,\mathrm{e}^{\mathsf{c}\,j}$ then $\mathsf{c} \leqslant 0$ will provide an estimate of the log-linear scaling as $\ln|\mathsf{g}(j) - \mathsf{a}| = \ln|\mathsf{b}| + \mathsf{c}\,j$.

Appendix F: The rate at the critical time

Here we begin with $|\psi_{\mathrm{in}}\rangle = |j\rangle_x$. For $h_{\mathrm{f}} = 0$, the Hamiltonian $H_{\mathrm{f}} = -\frac{1}{2N}(J_z)^2$ is diagonal in the basis $\mathcal{B}_z$ of (3), and the time evolved ket of (22) will be

$$|\psi(t)\rangle = \frac{1}{2^j}\sum_{m=-j}^{j}\binom{2j}{j+m}^{\frac{1}{2}} \exp\left(\mathrm{i}\,\frac{m^2}{4j}t\right)|m\rangle_z\,. \tag{F1}$$

With the coherent ket of (6), one can check that $|\psi(0)\rangle = |j\rangle_x$ and

$$|\psi(4j\pi)\rangle = \begin{cases} |-j\rangle_x & \text{when } j \in \mathbb{Z} \\ |+j\rangle_x & \text{when } j \in \mathbb{Z} + \frac{1}{2} \end{cases} \tag{F2}$$

up to a global phase factor, where $\mathbb{Z}$ and $\mathbb{Z} + \frac{1}{2}$ are the sets of integers and of half-integers, respectively. For an integer j, at the time $t = 4j\pi$, the phase factors in (F1) becomes $\exp\left(\mathrm{i}\,m^2\pi\right) = +1$ and -1 for an even and odd m, respectively. Therefore, we get $|-j\rangle_x$ in (F2). When $j \in \mathbb{Z} + \frac{1}{2}$, all the magnetic quantum numbers are of the form $m = k + \frac{1}{2}$, where $k \in \mathbb{Z}$. Consequently, $m^2 = k(k+1) + \frac{1}{4}$, and all the phase factors are the same $\exp\left(\mathrm{i}\,m^2\pi\right) = \exp\left(\mathrm{i}\,\frac{\pi}{4}\right)$ at $t = 4j\pi$, because $k(k+1)$ is an even number. As a result, we get $|+j\rangle_x$ in (F2).

Through (F2), we gain

$$\mathsf{x}(4j\pi) = \begin{Bmatrix} -1 & \text{when } j \in \mathbb{Z} & 0 \\ +1 & \text{when } j \in \mathbb{Z} + \frac{1}{2} & 1 \end{Bmatrix} = p(4j\pi)\,, \tag{F3}$$

where x is the x-component of the spin vector $\mathbf{s}$ of (23), and the return probability p is defined in (26). In fact, relations (F2) and (F3) hold true for any integral multiple of $t = 4j\pi$ as the motion is periodic [see Fig. 20], and $|\psi(8j\pi)\rangle = |+j\rangle_x$ when $j \in \mathbb{Z}$. Hence, we obtain the time period (41).

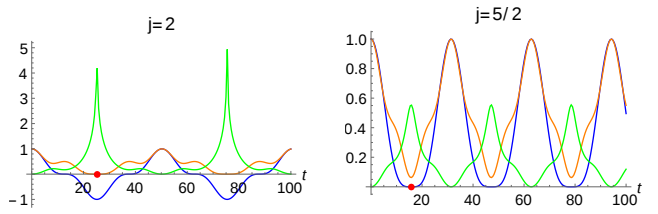

FIG. 20. The spin component, return probability, and rate versus time. The blue, orange, and green curves depicts the x-component of $\mathbf{s}$, the return probability p, and the Loschmidt rate r for $h_{\rm in}\to\infty$ and $h_{\rm f}=0$. The red points denote the half time periods $\frac{T}{2}=\tau$ given in (41).

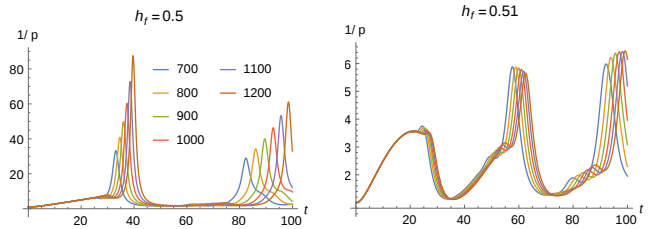

FIG. 21. Inverse probability versus time. Here $|\psi_{\rm in}\rangle=|j\rangle_x$, and $1/p$ of (26) is displayed in different colors for $j=700,\cdots,1200$. In comparison to a rate versus time plot, one can see a kink rather distinctly in a $1/p$ versus t plot such as this. In both the panels, the same color-coding is used, while the values of $h_{\rm f}$ are written at the top.

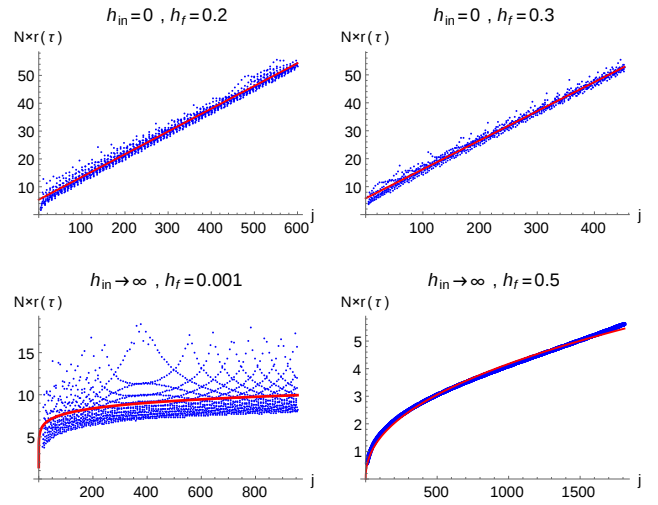

FIG. 22. Rate at the critical time versus system size. Plots in the top and bottom row are obtained by fixing $|\psi_{\rm in}\rangle=|j\rangle_z$ and $|\psi_{\rm in}\rangle=|j\rangle_x$, respectively. The top- and bottom-pictures are associated with the plots in Figs. 12 and 17, respectively. At each picture we place the values of the field strength for which the exact data $\{Nr(\tau_j)\}$ is obtained. Each data point is colored in blue. Recall that $N=2j$ is the system size and $r(\tau)$ is the value of Loschmidt rate (26) at the first critical time τ. The red curves show the best-fitted functions [registered in Table V] for the data.

TABLE V. The best fit functions for the rate at the critical time. This is the list of best fit functions for the data $\{Nr(\tau_j)\}$ presented in Fig. 22. The g-functions are illustrated by the red curves in the figure. In terms of MSE, one may get slightly better fit functions than those presented below.

$h_{\rm in}$	$h_{\rm f}$	g(j)	MSE
0	0.2	$5.35438+0.0817136\,j$	2.25784
0	0.3	$5.82377+0.103983\,j$	1.45764
∞	0.001	$4.67689\,j^{\,0.11}$	3.73926
∞	0.5	$0.186449\,j^{\,0.45}$	0.00510471

Furthermore, we acquire

$$\begin{aligned}\mathsf{x}(t)&=\frac{1}{j}\langle\psi(t)|J_x|\psi(t)\rangle\\&=\frac{1}{j}\,\frac{1}{2^{2j}}\sum_m\binom{2j}{j+m}(j-m)\cos\left(\frac{2m+1}{4j}t\right)\\&=\left(\cos\frac{t}{4j}\right)^{2j-1}.\end{aligned}\tag{F4}$$

As per (F4), we have $\mathsf{x}(2j\pi)=0$ for all $j\geqslant 1$, and x is a nonnegative function of t for every $j\in\mathbb{Z}+\frac{1}{2}$. Since J_z commutes with the final Hamiltonian here, we get

$$\begin{aligned}\langle\psi(t)|J_z|\psi(t)\rangle&=\langle\psi_{\rm in}|J_z|\psi_{\rm in}\rangle=0\\\langle\psi(t)|(J_z)^2|\psi(t)\rangle&=\langle\psi_{\rm in}|(J_z)^2|\psi_{\rm in}\rangle=\frac{j}{2},\ \text{and thus}\\\mathsf{m}=0\quad&\text{and}\quad\mathsf{m}'=\frac{1}{2j}\end{aligned}\tag{F5}$$

are the dynamical order parameters for every j.

In the case of a half-integer j, we discover that the probability p reaches it global minima at the first time $t=2\pi j$ [see Fig. 20]. Then the so-called Loschmidt amplitude becomes

$$\begin{aligned}\langle\psi_{\rm in}|\psi(2\pi j)\rangle&=\frac{1}{2^{2j}}\sum_m\binom{2j}{j+m}\exp\left(\mathrm{i}\,\frac{m^2}{2}\pi\right)\\&=\frac{2^{\,j+\frac{1}{2}}}{2^{2j}}\exp\left(\mathrm{i}\frac{\pi}{8}\right)\quad\text{and}\\p(2\pi j)&=\frac{2^{\,2j+1}}{2^{4j}}\approx\frac{1}{2^{2j}}\quad\text{for}\quad j\gg 1.\end{aligned}\tag{F6}$$

In Fig. 20, one can see that the first kink in the return rate $r(t)$ of (26) develops at the time τ when the probability hits its lowest value. So, from (F3) and (F6), we deduce the value of τ and report it in (41). Since $p=0$ in (F3), the rate diverges even for a finite $j\in\mathbb{Z}$ [see Fig. 20]. Whereas, for $j\in\mathbb{Z}+\frac{1}{2}$, we get $r(2\pi j)\approx\ln(2)$ for $j\gg 1$ from (F6). This completes the proof and discussion of (41).

Now we investigate the rate at the critical time $r(\tau)$. For $h_{\rm in}\to\infty$, we plotted the inverse of the probability $p(t)$ of (26) in Fig. 21. In the case of $h_{\rm f}=0.5$, one can observe that the peak at $t\approx 38$ gets higher and

sharper with the system size $N = 2j$. Whereas, in the case of $h_{\rm f} = 0.51$, the peak around $t = 23$ gets shorter and smoother with j. It demonstrates that there will be no kink in $r(t)$ for $h_{\rm f} > \frac{1}{2}$ (the regular phase) [69–71].

Recall that the height of the first kink is $r(\tau)$, and we present the rescaled rate $Nr(\tau) = \ln(\frac{1}{p(\tau)})$ in Fig. 22 for both Secs. III A and III B. In Table V, the best fit functions for these data-sets are given. In the case of Sec. III A, where $h_{\rm in} = 0$, the data $\{Nr(\tau_j)\}$ exhibit a linear behavior with j, which suggests $\lim_{j\to\infty} r(\tau_j)$ goes to a nonzero value for both $h_{\rm f} = 0.2, 0.3$. These two $h_{\rm f}$-values lie on the two sides of the dynamical critical point. In the case of Sec. III B, where $h_{\rm in} \to \infty$, the best fit function in Table V suggest $Nr(\tau_j) \sim \mathsf{b}\, j^{\mathsf{c}}$ where $0 < \mathsf{c} < 1$. It implies that $\lim_{j\to\infty} r(\tau_j)$ goes to zero with a power-law.

[1] S. Sachdev, *Quantum Phase Transitions* (Cambridge University Press, Cambridge, England 2011).
[2] H. J. Lipkin, N. Meshkov, and A. J. Glick, Nucl. Phys. **62**, 188 (1965).
[3] N. Meshkov, A. J. Glick, and H. J. Lipkin, Nucl. Phys. **62**, 199 (1965).
[4] A. J. Glick, H. J. Lipkin, and N. Meshkov, Nucl. Phys. **62**, 211 (1965).
[5] J. I. Cirac, M. Lewenstein, K. Mølmer, and P. Zoller, Phys. Rev. A **57**, 1208 (1998).
[6] A. Micheli, D. Jaksch, J. I. Cirac, and P. Zoller, Phys. Rev. A **67**, 013607 (2003).
[7] R. Botet, R. Jullien, and P. Pfeuty, Phys. Rev. Lett. **49**, 478 (1982).
[8] R. Botet and R. Jullien, Phys. Rev. B **28**, 3955 (1983).
[9] A. Das, K. Sengupta, D. Sen, and B. K. Chakrabarti, Phys. Rev. B **74**, 144423 (2006).
[10] M. E. Fisher and M. N. Barber, Phys. Rev. Lett. **28**, 1516 (1972).
[11] S. Hill and W.K. Wootters, Phys. Rev. Lett. **78**, 5022 (1997).
[12] W. K. Wootters, Phys. Rev. Lett. **80**, 2245 (1998).
[13] A. Shimony, Ann. N.Y. Acad. Sci. **755**, 675 (1995).
[14] H. Barnum and N. Linden, J. Phys. A **34**, 6787 (2001).
[15] M. B. Plenio and V. Vedral, J. Phys. A **34**, 6997 (2001).
[16] D. A. Meyer and N. R. Wallach, J. Math. Phys. **43**, 4273 (2002).
[17] T.-C. Wei and P. M. Goldbart, Phys. Rev. A **68**, 042307 (2003).
[18] A. Osterloh and J. Siewert, Phys. Rev. A **72**, 012337 (2005).
[19] A. Osterloh and J. Siewert, Int. J. Quant. Inf. **4**, 531 (2006).
[20] R. Orús, Phys. Rev. Lett. **100**, 130502 (2008).
[21] R. Orús, S. Dusuel, and J. Vidal, Phys. Rev. Lett. **101**, 025701 (2008).
[22] R. Orús, Phys. Rev. A **78**, 062332 (2008).
[23] M. Balsone, F. DellAnno, S. De Siena, and F. Illuminatti, Phys. Rev. A **77**, 062304 (2008).
[24] D. Z. Djoković and A. Osterloh, J. Math. Phys. **50**, 033509 (2009).
[25] Q.-Q. Shi, R. Orús, J. O. Fjrestad, and H.-Q. Zhou, New J. Phys. **12**, 025008 (2010).
[26] R. Orús and T.-C. Wei, Phys. Rev. B **82**, 155120 (2010).
[27] A. Sen (De) and U. Sen, Phys. Rev. A **81**, 012308 (2010).
[28] J. Vidal, G. Palacios, and R. Mosseri, Phys. Rev. A **69**, 022107 (2004).
[29] S. Dusuel and J. Vidal, Phys. Rev. Lett. **93**, 237204 (2004).
[30] S. Dusuel and J. Vidal, Phys. Rev. B **71**, 224420 (2005).
[31] S. Dusuel and J. Vidal, Phys. Rev. A **71**, 060304(R) (2005).
[32] R. Orús, S. Dusuel, and J. Vidal, Phys. Rev. Lett. **101**, 025701 (2008).
[33] J. I. Latorre, R. Orús, E. Rico, and J. Vidal, Phys. Rev. A **71**, 064101 (2005).
[34] T. Barthel, S. Dusuel, and J. Vidal, Phys. Rev. Lett. **97**, 220402 (2006).
[35] J. Vidal, S. Dusuel, and T. Barthel, J. Stat. Mech. (2007) P01015.
[36] J. Wilms, J. Vidal, F. Verstraete, and S. Dusuel, J. Stat. Mech. (2012) P01023.
[37] G. Liberti, F. Piperno, and F. Plastina, Phys. Rev. A **81**, 013818 (2010).
[38] P. Calabrese, F. H. L. Essler, and M. Fagotti, Phys. Rev. Lett. **106**, 227203 (2011).
[39] J. C. Halimeh, V. Zauner-Stauber, I. P. McCulloch, I. de Vega, U. Schollwöck, and M. Kastner, Phys. Rev. B **95**, 024302 (2017).
[40] G. Piccitto, B. Žunkovič, and A. Silva, Phys. Rev. B **100**, 180402(R) (2019).
[41] G. Piccitto, B. Žunkovič, and A. Silva, J. Stat. Mech. (2019) 094017.
[42] M. Eckstein, M. Kollar, and P. Werner, Phys. Rev. Lett. **103**, 056403 (2009).
[43] M. Schiró and M. Fabrizio, Phys. Rev. Lett. **105**, 076401 (2010).
[44] M. Schiró and M. Fabrizio, Phys. Rev. B **83**, 165105 (2011).
[45] M. Sandri, M. Schiró, and M. Fabrizio, Phys. Rev. B **86**, 075122 (2012).
[46] B. Sciolla and G. Biroli, Phys. Rev. Lett. **105**, 220401 (2010).
[47] M. Snoek, EPL **95**, 30006 (2011).
[48] B. Sciolla and G. Biroli, J. Stat. Mech. (2011) P11003.
[49] B. Sciolla and G. Biroli, Phys Rev B. **88**, 201110(R) (2013).
[50] A. Gambassi and P. Calabrese, EPL **95**, 66007 (2011).
[51] P. Smacchia, M. Knap, E. Demler, and A. Silva, Phys. Rev. B **91**, 205136 (2015).
[52] B. Žunkovič, A. Silva, and M. Fabrizio, Phil. Trans. R. Soc. A **374**, 20150160 (2016).
[53] A. Lerose, B. Žunkovič, J. Marino, A. Gambassi, and A. Silva, Phys. Rev. B **99**, 045128 (2019).
[54] B. Li, C. Gao, G. Xianlong, and P. Wang, J. Phys.: Condens. Matter **31**, 075801 (2019).
[55] J. Zhang, G. Pagano, P. W. Hess, A. Kyprianidis, P. Becker, H. Kaplan, A. V. Gorshkov, Z.-X. Gong, and C. Monroe, Nature (London) **551**, 601 (2017).
[56] J. A. Muniz, D. Barberena, R. J. Lewis-Swan, D. J. Young, J. R. K. Cline, A. M. Rey, and J. K. Thompson, Nature **580**, 602 (2020).

[57] K. Xu, Z.-H. Sun, W. Liu, Y.-R. Zhang, H. Li, H. Dong, W. Ren, P. Zhang, F. Nori, D. Zheng, H. Fan, and H. Wang, Sci. Adv. **6**, eaba4935 (2020).

[58] S. Smale, P. He, B. A. Olsen, K. G. Jackson, H. Sharum, S. Trotzky, J. Marino, A. M. Rey, and J. H. Thywissen, Sci. Adv. **5**, eaax1568 (2019).

[59] P. Jurcevic, H. Shen, P. Hauke, C. Maier, T. Brydges, C. Hempel, B. P. Lanyon, M. Heyl, R. Blatt, and C. F. Roos, Phys. Rev. Lett. **119**, 080501 (2017).

[60] M. Heyl, A. Polkovnikov, and S. Kehrein, Phys. Rev. Lett. **110**, 135704 (2013).

[61] M. Heyl, Phys. Rev. Lett. **115**, 140602 (2015).

[62] M. Heyl, Phys. Rev. Lett. **113**, 205701 (2014).

[63] J. C. Halimeh, M. Punk, and F. Piazza, Phys. Rev. B **98**, 045111 (2018).

[64] U. Bhattacharya, S. Bandyopadhyay, and A. Dutta, Phys. Rev. B **96**, 180303 (2017).

[65] S. Bhattacharjee and A. Dutta, Phys. Rev. B **97**, 134306 (2018).

[66] N. Defenu, T. Enss, and J. C. Halimeh, Phys. Rev. B **100**, 014434 (2019).

[67] S. Haldar, S. Roy, T. Chanda, A. Sen(De), and U. Sen, Phys. Rev. B **101**, 224304 (2020).

[68] J. C. Halimeh, M. V. Damme, V. Zauner-Stauber, and L. Vanderstraeten, Phys. Rev. Research **2**, 033111 (2020).

[69] J. C. Halimeh and V. Zauner-Stauber, Phys. Rev. B **96**, 134427 (2017).

[70] I. Homrighausen, N. O. Abeling, V. Zauner-Stauber, and J. C. Halimeh, Phys. Rev. B **96**, 104436 (2017).

[71] V. Zauner-Stauber and J. C. Halimeh, Phys. Rev. E **96**, 062118 (2017).

[72] B. Žunkovič, M. Heyl, M. Knap, and A. Silva, Phys. Rev. Lett. **120**, 130601 (2018).

[73] J. Lang, B. Frank, and J. C. Halimeh, Phys. Rev. Lett. **121**, 130603 (2018).

[74] J. Lang, B. Frank, and J. C. Halimeh, Phys. Rev. B. **97**, 174401 (2018).

[75] M. Heyl, Rep. Prog. Phys. **81**, 054001 (2018).

[76] A. Sen(De), U. Sen, and M. Lewenstein, Phys. Rev. A **72**, 052319 (2005).

[77] S. Deng, L. Viola, and G. Ortiz, Generalized entanglement in static and dynamic quantum phase transitions, *Recent Progress in Many-Body Theories*, Vol. **11** (World Scientific, Singapore, 2008), p. 387.

[78] H. S. Dhar, R. Ghosh, A. Sen(De), and U. Sen, Phys. Lett. A **378**, 1258 (2014).

[79] Y.-C. Lin, P.-Y. Yang, and W.-M. Zhang, Sci. Rep. **6**, 34804 (2016).

[80] S. Haldar, S. Roy, T. Chanda, and A. Sen(De), Phys. Rev. Research **2**, 033249 (2020).

[81] R. H. Dicke, Phys. Rev. **93**, 99 (1954).

[82] C. M. Newman and L. S. Schulman, J. Math. Phys. **18**, 23 (1977).

[83] F. T. Arecchi, E. Courtens, R. Gilmore, and H. Thomas, Phys. Rev. A **6**, 2211 (1972).

[84] J. S. Kim, G. Gour, and B. C. Sanders, Contemp. Phys. **53**, 417 (2012).

[85] H. S. Dhar, A. K. Pal, D. Rakshit, A. Sen(De), and U. Sen, Monogamy of quantum correlations - a review, in *Lectures on General Quantum Correlations and Their Applications*, Quantum Science and Technology, edited by F. F. Fanchini, D. de Oliveira Soares Pinto, and G. Adesso (Springer International Publishing, Berlin, 2017), pp. 23–64, (arXiv:1610.01069).

[86] X. Wang and K. Mølmer, Eur. Phys. J. D **18**, 385 (2002).

[87] D. M. Greenberger, M. A. Horne, and A. Zeilinger, e-print arXiv:0712.0921 [quant-ph].

[88] W. Dür, G. Vidal, and J. I. Cirac, Phys. Rev. A **62**, 062314 (2000).

[89] P. F. Byrd and M. D. Friedman, *Handbook of Elliptic Integrals for Engineers and Physicists* (Springer, New York, 1971), p. 11.